Diamond & Related Materials 146 (2024) 111245

Contents lists available at ScienceDirect

Diamond & Related Materials

journal homepage: www.elsevier.com/locate/diamond

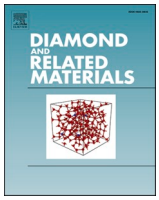

Newly synthesized Pb-based 312 MAX phases M_3PbC_2 (M = Zr and Hf): A First-principles study

M.R. Rana [a,b,1], S. Islam [a,b,1], K. Hoque [b], S. Mahmud [a,c], M.A. Ali [a,*]

[a] Advanced Computational Materials Research Laboratory (ACMRL), Department of Physics, Chittagong University of Engineering and Technology (CUET), Chattogram 4349, Bangladesh
[b] Physics Discipline, Khulnaa University, Khulna 9208, Bangladesh
[c] Department of Electrical and Electronic Engineering, Jatiya Kabi Kazi Nazrul Islam University, Mymensingh 2224, Bangladesh

ARTICLE INFO

Keywords:
312 MAX phases
DFT
Band structure
Mechanical properties
TBC material
Dynamical stability
Optical property

ABSTRACT

The MAX phases' unique mixture of ceramic and metallic features makes them appealing for various technological uses. Zr_3PbC_2 and Hf_3PbC_2, two Pb-based MAX phases, were recently synthesized experimentally. The physical properties, such as structural properties as well as electronic, mechanical, hardness, thermal, and lastly, the optical properties of M_3PbC_2 (M = Zr and Hf) have been investigated using density functional theory (DFT) and analogized with those of other 312 MAX phases. The optimized cell volume and computed lattice constants match the experimental values. The calculated band structure certifies the metallic character, and DOS calculations confirmed the dominant contribution to conductivity from the Zr-4*d* and Hf-5*d* states. The stiffness constant (C_{ij}) proved the mechanical stability of these compounds. The mechanical behavior of the studied compounds was explored by calculating the elastic moduli, hardness parameters, and fracture toughness, which are also compared to those of the 312 MAX phases. The tightly bound M–C covalent bonds within the crystal give these compounds high stiffness. The Mulliken population (both atomic and bond) was calculated to explore the bonding characteristics within them and the Vickers hardness of the titled phases. The degree of elastic anisotropy present within phases has been analyzed by calculating different indices. The phonon dispersion curves and phonon DOS (PHDOS) were computed to check the dynamical stability of the phases. Thermodynamic potential functions were calculated from the PHDOS. The thermal parameters were also studied, including the Debye temperature, melting temperature, Grüneisen parameter, and minimum thermal conductivity (K_{min}). A thorough computation and analysis of the vital optical constants was done to explore their potential in diverse fields. The titled compounds are suitable for use as thermal barrier coating (TBC) materials and coating materials to prevent solar heating.

1. Introduction

A family of substances called the MAX phases is now being researched for its unusual combination of features. For instance, compared with other carbides, they are machinable, flexible, and able to act in a plastic manner at a high temperature. These materials are intriguing for applications due to their combination of qualities, which has kept them in the public eye for the past few years [1]. Barsoum coined the phrase "$M_{n+1}AX_n$ phase" for the very first time in 2000 [1]. The generic formula $M_{n+1}AX_n$, subsequently abbreviated to '*MAX*' [2], included the following components: *M* stood for an earlier transition metal, *A* for a group 'A' element, *X* for C or N, and $n = 1–3$. This group of compounds has a crystal structure in the space group (number 194). It consists of layers of $M_{n+1}X_n$ and flat sheets containing A atoms positioned along the *c* direction [3]. The atoms within the $M_{n+1}X_n$ layers are held together by covalent bonds, making these layers ceramic-like, while the A atomic sheets have contributed to the metallic properties. These ceramic and metallic layers and sheets are arranged alternately along the *c*-axis, creating a mixture of ceramic-metallic characteristics found in MAX phases [4]. As the layer index '*n*' increases, MAX phases get several layers in their unit cell, compared to metallic sheets. Indeed, in the case of 211 MAX phases (where '*n*' equals one), a metallic sheet is sandwiched between two ceramic layers, and this pattern continues with '$n + 1$' ceramic layers separating each metallic sheet. The macroscopic

* Corresponding author.
E-mail address: ashrafphy31@cuet.ac.bd (M.A. Ali).
[1] First two authors contributed equally.

https://doi.org/10.1016/j.diamond.2024.111245
Received 15 March 2024; Received in revised form 21 May 2024; Accepted 26 May 2024
Available online 27 May 2024

properties are anticipated to be greatly impacted by large amounts of anisotropy. According to Barsoum and El-Raghy [5], the mechanical property is incredibly odd and consists of a mass movement of displacements in the basal plane that results in a kinking mechanism. This phenomenon has since been observed in a number of different materials, and it is thought to be rather typical for compounds with high *c/a* ratios. MAX phases exhibit specific metallic characteristics, including their ability to conduct electricity and heat, damage tolerance, ease of machining, relative ductility, thermal shock resistance, and plastic behavior at elevated temperatures [1]. Additionally, they possess ceramic attributes such as resistance to oxidation, exceptional refractoriness, high elastic stiffness, low density, and strong resistance to corrosion [3].

These materials possess a combination of stiffness (with Ti_3SiC_2 being approximately three times stiffer than titanium at a similar density [6]) and relative softness compared to binary carbide counterparts. This softness makes MAX phases amenable to machining with standard metalworking tools like hacksaws or lathes [7]. They are used in many applications, such as bond-coat layers of thermal barrier coating (TBC) systems, high-temperature materials, and automotive exhaust gas filters. Notably, their layered structure grants them impressive damage tolerance; the layers are capable of sliding, kinking, and delaminating to absorb deformations, resulting in localized hardening at the point of damage [8,9]. MAX phases are used as high-temperature burner nozzles, electric furnace components, and furnace tubes and have even been suggested for use as molds for latex gloves [6,10]. In nuclear-powered reactors, MAX phases are frequently used as neutron irradiation-resistant materials because of certain encouraging radiation tolerance investigations [11,12]. Due to their layered structure and self-lubricating qualities, they are contenders for bearing and other sliding purposes [13]. The utilization of MAX phases has gained popularity in generating their 2D counterpart known as "MXene." MXene is employed as a material for energy storage and serves as an electrode in micro-supercapacitors, batteries, and electrochemical capacitors [14]. Barsoum and El-Raghy initially created dense and phase-pure Ti_3SiC_2 in 1996, and through characterization, they demonstrated how it uniquely combined some of the most outstanding metal and ceramic engineering features [15]. The researchers then synthesize or theoretically forecast many MAX phases, including 312 MAX phases. Fang et al. [16] predicted V_3SiC_2 as a metastable compound, although it was suggested that it is possible to synthesize the compound as stable (or metastable) phases using thin-film deposition. Ti_3GaC_2 and Ti_3InC_2, synthesized by Cuskelly [17], showed that the *c*-axis length increased linearly with the radius of the atom of the A element. M. W. Barsoum et al. [18] explored the phase stability, compressibility, electronic, elastic, and optical properties of Ti_3SnC_2, whereas Rayhan et al. [19] studied the hardness and thermodynamic properties. Roknuzzaman et al. [20] investigated the first hafnium-based 312 MAX phase Hf_3AlC_2 and discovered the compound likely to be a superconducting phase. Fashandi et al. [21] synthesized Ti_3AuC_2, $Ti_3Au_2C_2$, and Ti_3IrC_2 by substitution reaction of noble metal in Ti_3SiC_2. They found that these phases create Ohmic electrical interactions with SiC and stay stable after 1000 h of aging at 600 °C in air. Ti_3SiC_2, Ti_3GeC_2, and Ti_3AlC_2 are explored by Chen et al. [22] and attested to the fact that, in high-temperature or radiation-prone environments, Ti_3AlC_2 is the most stable of the chosen M_3AC_2 materials. Ouadha et al. studied $(Zr_{1-X}Ti_X)_3AlC_2$ and investigated the fact that increasing pressure causes a significant increase in both the bulk modulus and the Debye temperature [23]. Rached et al. explored some MAX-phases. Some of them were found to be good candidates for TBC material, and some of them can be used in high-temperature applications as well as in nuclear industry applications [24–27]. Belkacem et al. also find that M_3GaC_2 (M = Ti & Zr) compounds have the potential to be used as TBC material [28]. Hadi et al. [29] explored that Ti_3ZnC_2 may be etched into 2D MXenes more readily than other Ti_3AC_2 compounds. Very recently, Hadi et al. [30] investigated the Sn-Based 312 MAX phases, where all the compounds can potentially be used as a coating material to prevent solar heating. Recently, two 312 MAX phases, Zr_3PbC_2 and Hf_3PbC_2, were synthesized experimentally by Zhang et al. [31].

After thoroughly analyzing the published reports in the previous section, we have discovered that the 312 MAX phases have the potential for practical applications, particularly in high-temperature technology. This has motivated us to further investigate the two synthesized MAX phases (Zr3PbC2 and Hf3PbC2) to determine if they can be utilized in this field. Although these two compounds were successfully synthesized by Zhang et al. [31], the physical properties and implications or potentiality of these compounds have not yet been addressed. To take full advantage of these compounds, the structural, electronic, and mechanical properties, including hardness, thermal, and optical properties, are explored within this work. Besides the studied properties, the authors highlight the significance of thermo-mechanical and optical properties in predicting Zr_3PbC_2 and Hf_3PbC_2 compounds as suitable materials for thermal barrier coatings (TBC) and coating material to reflect sunlight. A substance eligible for use as a TBC should possess exceptionally low thermal conductivity at elevated temperatures, high melting points, an extremely low thermal expansion coefficient, and adequate machinability to enable its application as a coating layer. The optical properties were considered to predict their (Zr_3PbC_2 and Hf_3PbC_2) suitability as coating materials to reduce solar heating.

Thus, this paper presents a first-time comprehensive report of the structural, electronic, mechanical, thermal, and optical properties of Zr_3PbC_2 and Hf_3PbC_2 compounds. The subsequent sections are arranged as follows: the computational methods in Section 2, the results and discussions in Section 3, the Environmental concern of the Pb-containing compounds in Section 4, and the conclusions and summarization of the findings in Section 5.

2. Computational methods

To perform the First-principles approach based on Density Functional Theory (DFT), the CASTEP code [32] has been used. Generalized gradient approximation (GGA), formed on the PBE-functional owing to Perdew-Burke-Ernzerhof, has been employed to treat the impact of exchange-correlation interactions [33–35]. The Vanderbilt ultra-soft pseudopotential has been used to evaluate electron-ion core interaction [36]. A *k*-point of 9 × 9 × 2-grid on the Monkhorst-pack scheme [37] with a plane wave cut-off energy of 550 eV is employed to create identical grid points within the reciprocal space. The Broyden–Fletcher–Goldfarb–Shanno (BFGS) relaxation arrangement optimizes the geometry by limiting the total energy and the internal forces [38]. Atoms are positioned more loosely to converge on the way to an overall energy difference of <5 × 10–6 eV/atom; maximum force, stress, and ionic displacement are taken in between 0.01 eV/Å, 0.02 GPa, and 5 × 10^{-4} Å correspondingly. We derived the elastic constants using the "stress-strain" technique built into the CASTEP program. The elastic moduli have been calculated using the anticipated elastic constant tensors C_{ij}. The phonon dispersions were computed using the DFPT linear-response approach [39]. The quasi-harmonic Debye approximation was applied to acquire the thermodynamic properties from the phonon density of states.

3. Results and discussions

3.1. Structural properties

The 312 MAX family contains the recently synthesized Zr_3PbC_2 and Hf_3PbC_2, which crystallize within the hexagonal space group $P6_3/mmc$ (No. 194). Fig. 1(a) displays the unit cell of the phases under study. At the very center of the triangle prism in the structure, the square-planar tiles of the Pb-atom's atomic layers coincide with the almost closed-packed layers of M_6C (M = Zr or Hf) octahedra. C atoms dwell in the octahedral sites located between M atoms. Fig. 1(b) shows the stacking

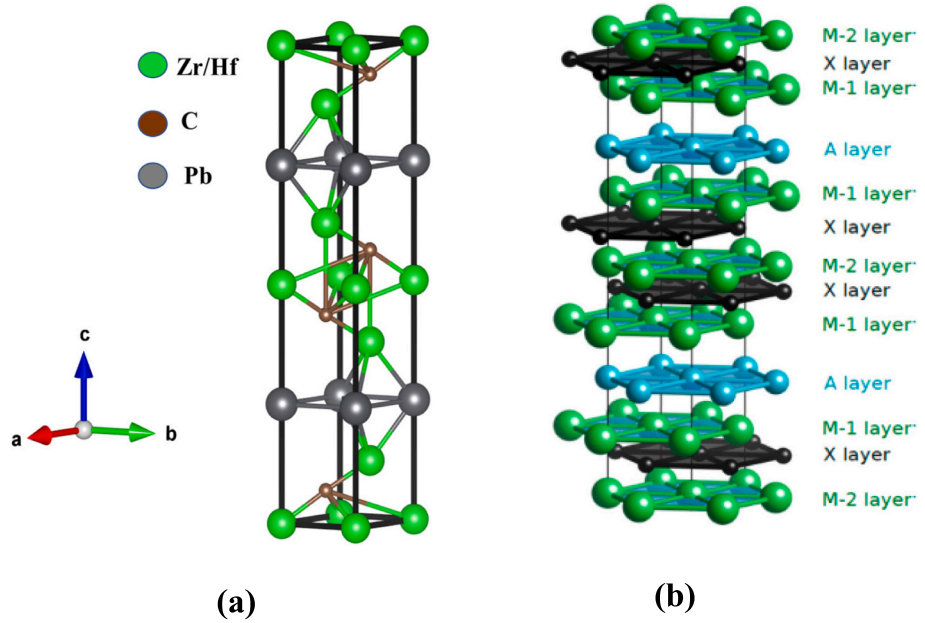

Fig. 1. Structural features: (a) the unit cell of the M_3PbC_2 (M = Zr and Hf) compounds and (b) the stacking of layers in 312 MAX phases [40].

of layers in 312 MAX phases, the layers stacked along the *c*-direction. The MX slab is formed by enclosing an 'X' layer with 'M' layers with a face-centered-cubic-type stacking sequence. The 'A' layers act as separators between these slabs. Moreover, there is an HCP stacking pattern around the 'A' layers, where the 'A' layers themselves form a mirror plane within the crystal. Table 1 lists the optimized lattice parameters of the phases under study, experimental values, and the other 312 MAX phase carbides. The structural parameters have slightly higher values compared to the other compounds that were previously investigated, as mentioned in Table 1.

Using the c/a ratio and the internal parameter Z_M, the distortion parameters for the unit cell structure have been computed. An optimum structure has octahedron (O_r) and trigonal (P_r) parameters that are equal ($O_r = P_r = 1$); deviations from 1 for O_r and P_r denote distortion in the polyhedral structures. A structure with less distortion represents more stability [41]. The O_r and P_r can be calculated by using the following formulae:

$$O_r = \frac{\sqrt{3}}{2\sqrt{4z_M^2\left(\frac{c}{a}\right)^2 + \frac{1}{12}}} \text{ and } P_r = \frac{1}{\sqrt{\frac{1}{3} + \left(\frac{1}{4} - z_M\right)^2\left(\frac{c}{a}\right)^2}} \quad (1)$$

O_r (P_r) values for Zr_3PbC_2 and Hf_3PbC_2 are 0.568 (1.058) and 0.569 (1.073), respectively. This indicates that the distortion in the analyzed structures for octahedron and trigonal prisms is relatively similar because of the extremely closed value of ratios (O_r/P_r).

Table 1 lists the (Or/Pr) ratios for the phases under study. The studied compounds are less distorted than the others.

Table 1
Data for structural parameters of M_3PbC_2 (M = Zr and Hf) compounds.

Phase	a (Å)	c (Å)	Z_M	c/a	V (Å^3)	O_r/P_r
Zr_3PbC_2	3.394	20.315	0.125	5.99	202.62	0.537
Zr_3PbC_2 (exp)[a]	3.377	20.007	0.126	5.92	197.6	0.53
Zr_3SnC_2[b]	3.369	20.04	0.128	5.949	197	0.53
Hf_3PbC_2	3.398	20.092	0.126	5.91	200.97	0.53
Hf_3PbC_2 (exp)[a]	3.336	19.77	0.126	5.926	190.5	0.53
Hf_3SnC_2[b]	3.373	19.829	0.1296	5.878	195.4	0.51
Ti_3AlC_2[c]	3.0786	18.73	–	6.08	153.736	–
Ti_3AlC_2[d]	3.0705	17.725	–	5.7727	144.725	–

[a] Reference [31].
[b] Reference [42].
[c] Reference [43].
[d] Reference [29].

3.2. Electronic properties

3.2.1. Band structure

The band structure provides vital information regarding electrical behavior. Fig. 2 displays the predicted band structures of Zr_3PbC_2 and Hf_3PbC_2 compounds along the high symmetry points in *k*-spaces. The dashed line in both figures indicates the Fermi level, E_F, at zero energy levels. At E_F, there is an overlap in the *K*-Γ and *K*-Γ directions of both the valance band and conduction band; due to the overleaping, no band gap exists, representing the compound's metallic nature. Additionally, the band structures of both Zr_3PbC_2 and Hf_3PbC_2 demonstrate the anisotropic character of electronic conductivity. An identical result was divulged by Roknuzzaman et al. [20] for Hf_3AlC_2. The electron energy dispersion is illustrated along the c-axis for the pathways Γ-A, H—K, and M-L, while it is depicted in the basal planes for the paths A-H, K-Γ, Γ-M, and L-H. Analysis of Fig. 2 reveals that the energy dispersion in the c-direction surpasses that in the basal plane due to the larger effective mass of electrons in the c-direction [44]. The reduced energy dispersion along the c-axis enables a clearer observation of the anisotropy in electrical conductivity. Consequently, the conductivity across the c-axis is anticipated to be lower than in the basal planes. Usually, the cubic materials are isotropic, while the hexagonal or layered structured materials are anisotropic owing to the differences in the atomic arrangement along the c-direction and basal plane. The anisotropic behavior of

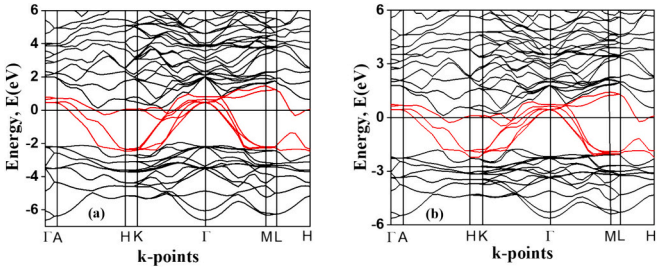

Fig. 2. Band structure of (a) Hf_3PbC_2 and (b) Zr_3PbC_2 compounds.

materials is frequently leveraged in electronic devices to optimize performance or achieve specific functionalities.

3.2.2. Density of state (DOS)

The total and partial DOS of Zr_3PbC_2 and Hf_3PbC_2 have also been calculated to assess the involvement of the electronic states to electronic conductivity, shown in Fig. 3, with the Fermi energy level indicated by the dashed line. According to the graphs, the densities of states (DOS) at the Fermi level (E_F) for Zr_3PbC_2 and Hf_3PbC_2 are 3.5498 and 3.6823 states per *eV* per unit cell, respectively. The Zr-*d* and Hf-*d* states are primarily responsible for this DOS at the Fermi level. This *d*-resonance and the non-zero DOS value at the Fermi level indicate the metallic conductivity of the ternary compounds Zr_3PbC_2 and Hf_3PbC_2. The orbital hybridizations that these compounds share are shown in Fig. 3. This includes interactions between the *d* orbitals of element M and the *p* orbitals of Pb or C, located at energy levels lower or higher than the Fermi energy, known as bonding (or anti-bonding) interactions. The 'M' atom also shows nonbonding states near the Fermi energy level. These substances contain the Fermi energy within a pseudo gap, separating the bonding and nonbonding states.

The bonding states are filled in the case of Zr_3PbC_2 and Hf_3PbC_2 compounds, whereas the nonbonding states are only slightly occupied. This causes the Fermi energy to move to a higher energy area and causes the number of states at the Fermi energy to quickly increase. Structural stability is often diminished when insufficient valence electrons populate the anti-bonding states or, conversely, an excessive number of extra electrons fill the bonding states. However, there is little to no impact on the structure's stability when nonbonding states are occupied. [45]. These findings allow us to conclude that the Zr_3PbC_2 and Hf_3PbC_2 compounds are stable. The valence band is partitioned into three discernible sections: the lowest valence band (LVB), covering −12 to −8.22 eV for Zr_3PbC_2 and −13 to −9.15 eV for Hf_3PbC_2, dominated by C-*s* orbitals with minor Pb-*s*, M-*d*, and M-*p* state involvement; the mid valence band (MVB) within −5.7 to −2.23 eV for Zr_3PbC_2 and −6.63 to −2.61 eV for Hf_3PbC_2, characterized by robust C-*p* and M-*d* hybridization; and the upper valence band (UVB) spanning −1.4 to 0.0 eV for Zr_3PbC_2 and −1.54 to 0.0 eV for Hf_3PbC_2, featuring a noteworthy M-*d* and C-*p* affinity at lower energy levels, in contrast to a closer M-*d* and Pb-*p* relationship near the Fermi energy (E_F), revealing distinct electronic interactions within Zr_3PbC_2 and Hf_3PbC_2 compounds. The dominant contributors to electronic conduction at the Fermi level are primarily the Zr-4*d* and Hf-5*d* electrons. In contrast, the involvement of Pb and C atoms in conduction is notably limited, although they do exhibit a slight presence in the TDOS at the Fermi level. This conclusion aligns with the results indicating that alterations in the M site substantially affect resistivity [46,47]. In contrast, replacements at the 'A' or 'X' sites have a comparatively lesser impact [48]. Qu et al. [49] have determined that the Ti-*d* electrons drive the electronic conduction at the Fermi level in the Ti_3SiC_2 compound.

3.2.3. Charge density mapping

The charge density mapping (in units of $e/Å^3$) along the (101) crystallographic plane is shown in Fig. 4 to assess bond strength and comprehend the characteristics of the bond between different atoms. The plot's right-hand side displays the color scale. Yellow-blue plot zones denote the areas of charge depletion, while red zones denote charge accumulation regions. Unevenly distributed negative or positive charges at the atomic sites result in the formation of an ionic bond. In contrast, the preferential accumulation of charges (positive areas) among two atoms forms a covalent bond [50]. The two compounds exhibit strong M-C (Zr—C and Hf—C) covalent bonding, as evidenced by the charge density patterns around the 'C' and 'Pb' atoms, which are relatively spherical, and the distorted distribution around the 'M' atom towards 'C' atoms. Furthermore, C's almost spherical charge distribution towards Pb indicates the ionic character of the Pb—C bonding.

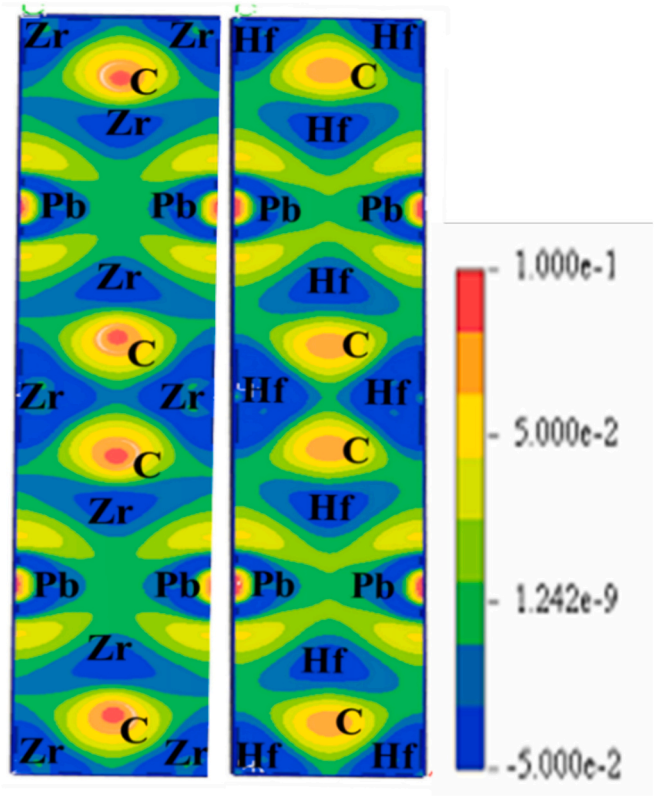

Fig. 4. Charge density mapping of Zr_3PbC_2 and Hf_3PbC_2.

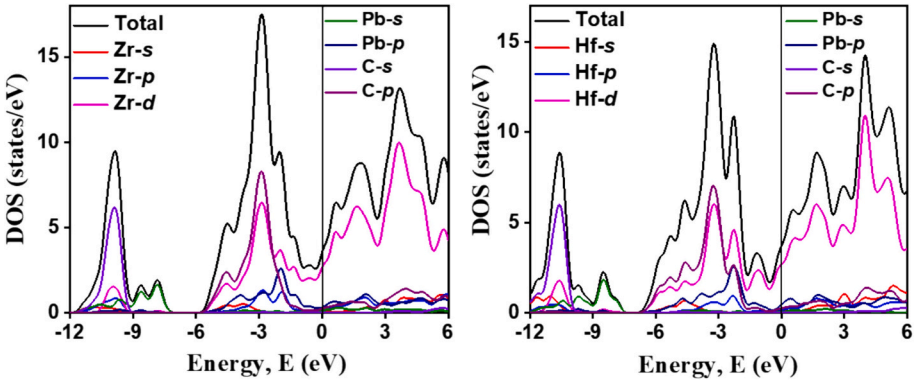

Fig. 3. Diagram for density of state of (a) Hf_3PbC_2 and (b) Zr_3PbC_2 compounds.

3.3. Mechanical properties

The mechanical response of materials relies on their elastic constants, which, in turn, are intertwined with the bonding characteristics of the materials. As a result of the inherent relationship between elastic properties and bonding characteristics, the insights provided by elastic constants are strongly related to the chemical bonds between the atoms in the solid. The relationship between the material's stress σ_i and the applied strain α_j is established by the elastic constants C_{ij}. The stress-strain method, which includes fitting calculated stresses of elongated cells to the following equation, was used to determine C_{ij}.

$$\sigma_i = \sum_{ij} C_{ij}\alpha_j\xi_j \tag{2}$$

Due to the hexagonal shape of MAX phase compounds [51,52], similar to other materials of this type, the 312 MAX phase possesses six distinct elastic constants: C_{11}, C_{12}, C_{13}, C_{33}, C_{44}, and C_{66}, with the first five being independent. At the same time, C_{66} relies on the relationship $C_{66} = (C_{11} - C_{12}) / 2$. For the MAX compounds to attain mechanical stability, the following criteria must be satisfied [53]:

$$C_{11} > |C_{12}|; C_{44} > 0; C_{66} > 0; (C_{11} + C_{12})C_{33} > 2C_{13}^2 \tag{3}$$

Table 2 shows that the elastic constants we computed fully meet these requirements, confirming the mechanical stability of both Zr_3PbC_2 and Hf_3PbC_2.

The C_{ij} values also offer valuable insights into the mechanical properties of the Zr_3PbC_2 and Hf_3PbC_2 MAX phases under investigation. For example, the C_{11} and C_{33} coefficients signify the stiffness of a material when subjected to stress along the (100) and (001) crystallographic directions, respectively. On the other hand, the C_{44} coefficient quantifies the material's resistance to shear deformation inside the (100) crystallographic plane. The C_{44} value is smaller than the unidirectional stiffness constants C_{11} and C_{33}, suggesting that the shear deformation is more favorable than linear compression along the *a*- and *c*-axes.

The C_{11} and C_{33} coefficients of Zr_3PbC_2 and Hf_3PbC_2 are greater than that of C_{44}, indicating a lower resistance to shear deformation as compared to unidirectional deformation. Zapata-Solvas et al. [4] also reported a similar finding in their study involving synthesizing a Zr-containing 312 MAX phase. The observed disparity in bonding strength between the [100] and [001] directions can be ascribed to the higher value of C_{11} compared to C_{33}. The Zr_3PbC_2 and Hf_3PbC_2 compounds exhibit anisotropic compressibility, with greater resistance to compression observed along the crystallographic *a*-axis than the *c*-axis. The uneven values of C_{11} and C_{33} further evidence anisotropic bonding strength along the *a*-axis and *c*-axis. The magnitudes of the C_{12} and C_{13} are somewhat less when compared to the remaining single-crystal elastic constants. The combination of these two elements involves the application of stress along the *a*-axis and the occurrence of uniaxial strain along the *b*- and *c*-axes, respectively. Once more, it can be inferred from the inequality $C_{11} + C_{12} > C_{33}$ that the bonding strength and tensile elastic modulus are larger in the (001) plane compared to the direction along the *c*-axis.

Utilizing elastic constants enables the estimation of specific micromechanical parameters in polycrystalline specimens, including the bulk modulus, shear modulus, and Young's modulus. The bulk modulus, denoted as *B*, quantifies the magnitude of inter-atomic bonding and the capacity of solids to withstand changes in volume, where the shear modulus *G* is a parameter that can be employed to elucidate the ability of a material to withstand transverse (plastic) deformations. Additionally, it can measure the average shear ability of a specific material. The widely recognized Voigt-Reuss-Hill (VRH) approximation, as documented in references [54–56], is employed to determine the elastic properties of the polycrystalline carbide material. Table 2 presents the computed elastic moduli of the studied compounds in contrast to other 312 MAX phase carbides based on Zr and Hf, and these theoretical values of elastic moduli are very analogous to the experimental work of Zr_3PbC_2 and Hf_3PbC_2 compounds [31].

The elevated value of *B* signifies the material's notable capacity to resist compression. The compressibility of a material can be evaluated by considering the reciprocal value of its B. In this context, a material with a low *B* value exhibits higher compressibility. The Zr_3PbC_2 compound has the most pronounced characteristic of having the lowest value of *B*, resulting in the lowest resistance when subjected to compression.

On the contrary, Hf_3PbC_2, exhibiting the utmost magnitude, demonstrates the greatest resistance to compression. Furthermore, it has been shown that the bulk moduli of Zr_3PbC_2 and Hf_3PbC_2 are comparatively smaller when compared to other MAX phases containing zirconium and hafnium. Shear modulus can also be used to measure the stiffness of materials. A high value of *G* signifies the hardness of the compounds, whereas a low value of *G* indicates its softness. The shear modulus (*G*) for Zr_3PbC_2 is significantly greater than that of Hf_3PbC_2. This disparity suggests that Zr_3PbC_2 shows a higher hardness level than Hf_3PbC_2. However, when compared to other MAX phases containing Zr and Hf, such as those listed in Table 2, it can be shown that Zr_3PbC_2 and Hf_3PbC_2 are less hard. Young's modulus (*Y*) is a physical property that

Table 2
Data for the stiffness constants, elastic moduli, Poisson's ratio (υ), Pugh's ratio (G/B), machinability (B/C_{44}), *f*-index, hardness parameters, and fracture toughness (K_{IC}) of M_3PbC_2 (M = Zr and Hf) compounds.

Parameters	Zr_3PbC_2	Hf_3PbC_2	Ti_3AlC_2[a]	Ti_3SiC_2[b]	Zr_3AlC_2[c]	Hf_3AlC_2[d]
C_{11} (GPa)	275	284	355[a]	370[b]	322[c]	347[d]
C_{12} (GPa)	83	107	84[a]	97[b]	73[c]	77[d]
C_{13} (GPa)	72	77	76[a]	112[b]	75[c]	80[d]
C_{33} (GPa)	237	238	292[a]	349[b]	270[c]	291[d]
C_{44} (GPa)	73	76	119[a]	155[b]	106[c]	127[d]
B (GPa)	138	146	163[a]	192[b]	151[c]	162[d]
G (GPa)	85	84	125[a]	140[b]	113[c]	127[d]
Y (GPa)	212	211	299[a]	338[b]	272[c]	302[d]
υ	0.243	0.258	0.194[a]	0.207[b]	0.20[c]	0.189[d]
B/G	1.62	1.74	1.304	1.37	1.34	1.276
G/B	0.62	0.57	0.77	0.73	0.75	0.78
B/C_{44}	1.87	1.91	1.37	1.24	1.42	1.28
f	1.30	1.47	1.33	1.03	1.26	1.25
H_{macro} (GPa)	12.34	10.99	21.83	21.92	19.69	22.44
H_{micro} (GPa)	14.57	13.55	27.68	29.1	22.67	26.33
K_{IC} (MPa $m^{1/2}$)	1.74	1.78	3.3	3.7	3.1	3.4

[a] Reference [57].
[b] Reference [57].
[c] Reference [58].
[d] Reference [20].

quantifies the tensile stiffness of a solid material. Recently synthesized compounds Zr_3PbC_2 and Hf_3PbC_2 exhibit a comparable Y value. So, the stress necessary for the deformation of Zr_3PbC_2 and Hf_3PbC_2 is almost equal. The relationship between Young's modulus of MAX phases and the exfoliation energy may be established. As the Y value decreases, the material exhibits a softer nature, resulting in a decrease in exfoliation energy and an increase in the likelihood of etching into 2D MXenes [59]. The elastic constants and elastic moduli of Zr_3AlC_2, Hf_3AlC_2, Ti_3SiC_2, and Ti_3AlC_2 are also presented in Table 2 and plotted in Fig. 5 for comparison. As seen, the values of the parameters of Pb-containing phases are lower than those of others given here. Strong metallic or covalent bonds are typically associated with higher elastic moduli and elastic constants in materials. Table 4 illustrates that Zr—C and Hf—C have weaker bonds than Ti—C (a longer bond implies a weaker bond), which results in a lower hardness value for the compounds under investigation.

The machinability index is a significant measure utilized to evaluate the machinability of substances. The quality in question is defined by the bulk modulus B and the shear elastic constant C_{44}. The machinability index, as determined by Sun et al. [60], is represented by the equation $\mu = B/C_{44}$. A material that can be used in various shapes or forms must have a high value for this parameter. As shown in Table 2, the values of C_{44} of Pb-based 312 phases are much lower than the previously studied Al and Si-based 312 phases, representing the lower resistance to shear deformation along (100) direction, resulting in the high machinability index, which gives the priority of being used in the machining process to these Pb-based 312 phases. The prediction of a compound's ductile and brittle characteristics can be achieved by an alternative method known as Pugh's modulus, which is calculated as the ratio of B/G or G/B. More analytically, it can be observed that when the ratio of Pugh's parameter (G/B) is <0.57 or the reciprocal of this ratio (B/G) is >1.75, the material can be classified as ductile. The B/G is 1.62 for Zr_3PbC_2 ($G/B = 0.62$) and 1.74 for Hf_3PbC_2 ($G/B = 0.575$), which is <1.75 (B/G is >0.57), thus, the titled phases are brittle. It should be noted that the brittleness index of Hf_3PbC_2 is very close to the borderline, which implies less brittle and more machinable, as seen from B/C_{44} values. This means that the propagation of cracks occurs at a high rate, even with minimal external tension exerted on the material.

Poisson's ratio, denoted as υ, is a significant characteristic of polycrystalline aggregates, offering valuable insights into the mechanical characteristics of crystalline materials. Poisson's ratio, Cauchy pressure, and Pugh's ratio may be used to anticipate the stability of materials in response to shear forces. The Poisson's ratio can be determined by using the equation $\upsilon = (3B - 2G)/(6B + 2G)$, where, υ represents the Poisson's ratio, B denotes the bulk modulus, and G represents the shear modulus. Frantsevich et al. [61] introduced a critical threshold of $\upsilon \sim 0.26$ to distinguish between materials exhibiting brittle and ductile behavior. The υ for the Zr_3PbC_2 and Hf_3PbC_2 compounds was determined to be 0.24384 and 0.25891, respectively, based on the data shown in Table 2. Both compounds are characterized by brittleness. The use of υ extends to t evaluating interatomic forces inside crystals [62]. If the υ of a crystalline solid falls within the range of 0.25–0.50, it may be inferred that the central forces exerted inside the solid are effective. The interatomic forces will exhibit non-central characteristics if the υ falls beyond this range. In the case of Hf_3PbC_2, the interatomic forces are governed mainly by non-central forces, but in the case of Zr_3PbC_2, the interatomic forces are predominantly influenced by central forces. Furthermore, the υ is crucial in evaluating the chemical bonding characteristics inside crystalline structures. When the value of υ is equal to or <0.1, a material may be characterized by covalent bonds. On the other hand, when the value of υ is equal to or >0.33, the atomic bonding in the material is attributed to metallic bonds [63]. The 312 MAX phases that were investigated exhibit Poisson's ratio within the range of these typical values. As a result, the MAX phases under investigation are expected to have a predominant presence of metallic and covalent bonding. By using the crystalline elastic modulus, we can calculate the hardness of the Zr_3PbC_2 and Hf_3PbC_2 compounds, respectively, from the following equations, $H_{macro} = 2\left[\left(\frac{G}{B}\right)^2 G\right]^{0.585} - 3$ [64–66] and $H_{micro} = \frac{(1-2\upsilon)Y}{6(1+\upsilon)}$ [67–69]. Table 2 represents the calculated values of H_{macro} and H_{micro} for the Zr_3PbC_2 and Hf_3PbC_2 compounds, which indicates their hardness as a measure of their ability to withstand external loads. As seen in Table 2, the value of these parameters of the studied compounds is lower than those of the other mentioned 312 MAX phases, which is expected. As mentioned in the above equations, these parameters are based on the value of the elastic moduli; the lower the elastic moduli, the lower the hardness parameters. The elastic moduli are lower than those of other mentioned compounds, which results in the lower value of these hardness parameters.

For the purpose of mechanical applications, we also calculated the fracture toughness (K_{IC}) of Zr_3PbC_2 and Hf_3PbC_2 compounds, which

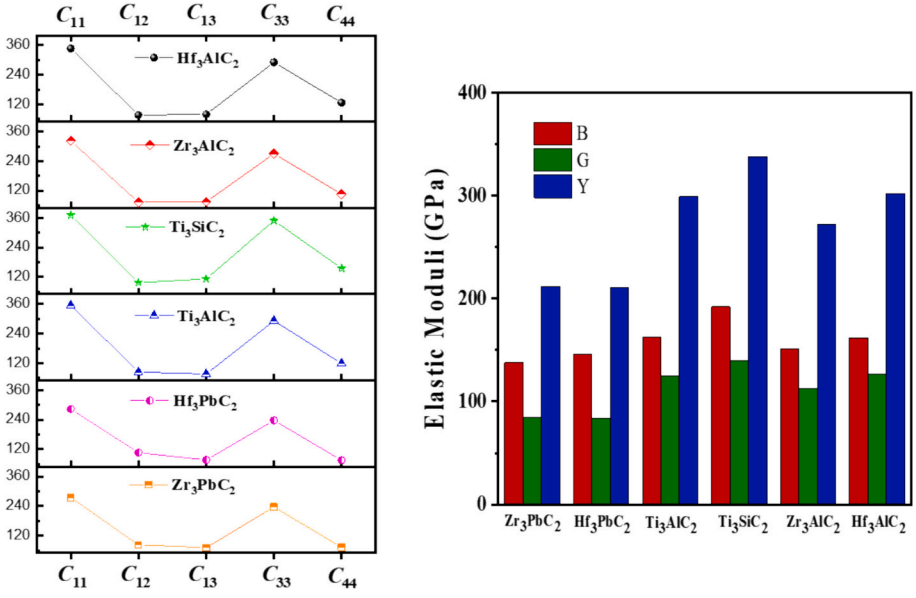

Fig. 5. Graphical representation of the stiffness constants (Left) and the elastic moduli (Right) of the studied compounds with previously explored compounds.

define the resistance to crack extension. Like hardness parameters, K_{IC} also depends on the elastic moduli, which causes a decrease in the value of this parameter in comparison to the other 312 MAX phases mentioned in Table 2. We found the K_{IC} values of Zr_3PbC_2 and Hf_3PbC_2 are 1.74 MPa $m^{1/2}$ and 1.78 MPa $m^{1/2}$, respectively, and these values are relatively close to the fracture toughness of the segmented YSZ coating in the range of 2.0–2.3 MPa $m^{1/2}$ [70,71].

The *f*-index, defined as the linear compressibility ratio along the *a*-axes and *c*-axes, is another significant factor that examines the bonding strength and degree of isotropic nature along these axes [72].

$$f = \frac{(C_{11} + C_{12} - 2C_{13})}{(C_{33} - C_{13})} \tag{4}$$

Bonds are isotropic along the *a*- and *c*-axes if $f = 1$ and stiffer in the *ab*-plane as compared to the c-direction if $f > 1$. When exposed to a particular mechanical strain, such as ultrasonic excitation, a larger f (>1) may be linked to a higher probability of the material exfoliating into 2D nanosheets. The value of the *f*-index of the studied compounds is slightly larger than other compounds mentioned in Table 2, demonstrating that they have a higher possibility of exfoliation than other compounds. The exfoliation of Ti_2AlC ($f = 1.174$) has already occurred [14], so Zr_3PbC_2 ($f = 1.297$) and Hf_3PbC_2 ($f = 1.47$) would be the candidates for experimental exfoliation.

3.3.1. Mulliken population

The primary information source for Mulliken atomic populations in the linear combination of atomic orbitals-molecular orbital (LCAO-MO) theory system is first-order electron density functions [65,73,74]. Sanchez-Portal et al. [75] modified the CASTEP code to support Mulliken atomic populations by jutting plane-wave states upon a linear combination of atomic orbitals (LCAO). Mulliken population analysis in non-magnetic systems produces Mulliken bond populations, Hirshfeld charges, and Mulliken charges. The formulas provided below are utilized to compute the Mulliken charge (α) linked with a specific atom [73], $\mathscr{C}(\alpha) = \sum_k w_k \sum_\mu^{on\ \alpha} \sum_\upsilon P_{\mu\upsilon}(k) S_{\mu\upsilon}(k)$ and the bond population involving two atoms α and β is [73], $P(\alpha\beta) = \sum_k w_k \sum_\mu^{on\ \alpha} \sum_\upsilon^{on\ \beta} 2P_{\mu\upsilon}(k) S_{\mu\upsilon}(k)$, where $P_{\mu\upsilon}$ denotes the density matrix elements and $S_{\mu\upsilon}$ denotes the overlap matrix.

Fractional electron distribution across various atomic bond regions is examined through Mulliken population analysis. Understanding the nature of atomic bonding comprehensively requires analyzing the Mulliken atomic population and effective valence charge [76].

The effective valence charge conveys information about a chemical bond's covalent or ionic properties and strength. Atoms with a non-zero effective valence charge prefer forming covalent bonds, with values significantly larger than zero indicating the degree of covalency. Table 3 highlights prominent covalent bonds in Zr_3PbC_2 and Hf_3PbC_2 compounds, as evidenced by effective valence charge values exceeding zero. Additionally, the overlap population is a valuable criterion for assessing atom-to-atom bonding and determining the covalent or ionic nature of a bond. A small bond population's value signifies an ionic interaction, while a large value denotes a covalent bond [77]. In the studied compounds, Zr_3PbC_2 and Hf_3PbC_2 each form four bonds: C—Zr1, C—Zr2 and C—Hf1, C—Hf2, among those C—Zr1 and C—Hf1 bonds exhibit greater covalency than the other two bonds due to higher bond population values. Table 3 also reveals positive Mulliken charges for Zr and negative charges for C/Pb in the Zr_3PbC_2 compound, indicating charge transfer from Zr to C/Pb. Similarly, in the Hf_3PbC_2 compound, charge transfer from Hf and Pb to C is also observed.

3.3.2. Theoretical Vickers hardness

The hardness of a solid reflects its resistance to plastic deformation, dent, excess, and scrabbling [20]. It is a critical mechanical property among solid materials, significantly influencing the choice of materials for various engineering applications [42]. Gao [78] proposed a theorem for determining the theoretical Vickers hardness of nonmetallic compounds; however, this method proved ineffective for determining the Vickers hardness of partially metallic compounds, such as MAX phase compounds [79]. In response to this limitation, Gao and colleagues [79] introduced a novel term known as "metallic populations" to assess the Vickers hardness of metallic materials. Additionally, they modified Gao's equation to calculate bond hardness, resulting in the following formulation:

$$H_v^\mu = 740(P^\mu - P^{\mu'})\left(v_b^\mu\right)^{(-5/3)} \tag{5}$$

The Mulliken overlap population of the μ-type bond is denoted as P^μ, while $P^{\mu'}$ is introduced for the metallic population. The utilization of unit cell volume (V) and the total number of free electrons in a cell $n_{free} = \int_{E_P}^{E_F} N(E)dE$ brings $P^{\mu'}$ into action, calculated as $P^{\mu'} = n_{free}/V$, where E_P represents the energy at pseudogap. The volume of a bond of the μ-type, v_b^μ, is determined by the bond length d^μ of the μ-type and the number of bonds N_b^ν of type ν per unit volume, given by the equation $v_b^\mu = (d^\mu)^3 / \sum_\nu \left[(d^\mu)^3 N_b^\nu\right]$. To assess the hardness of complex multiband crystals, the geometric mean of all bond harnesses can be determined using the following equation [80]:

Table 3
Data for Mulliken atomic populations and effective valence charge of M_3PbC_2 (M = Zr, Hf) compounds.

Compound	Atom	Mulliken atomic population					Effective valance charge
		s	*p*	*D*	Total	Charge	
Zr_3PbC_2	C	1.50	3.29	0.00	4.79	−0.79	–
	Pb	1.44	2.58	10.04	14.05	−0.05	3.95
	Zr1	2.27	6.58	2.73	11.58	0.42	3.58
	Zr2	2.16	6.44	2.61	11.21	0.79	3.21
Hf_3PbC_2	C	1.55	3.32	0.00	4.87	−0.87	–
	Pb	1.01	2.67	10.04	13.71	0.29	3.71
	Hf1	0.45	0.41	2.82	3.68	0.32	3.68
	Hf2	0.39	0.04	2.75	3.17	0.83	3.17
Hf_3AlC_2[a]	C	1.56	3.32	0.00	4.88	−0.88	–
	Al	1.17	1.99	0.00	3.15	−0.15	2.85
	Hf 1	0.40	−0.02	2.74	3.12	0.88	3.12
	Hf 1	0.41	0.30	2.77	3.48	0.052	3.48
Ti_3AlC_2[b]	C	1.48	3.25	0.00	4.73	−0.73	–
	Al	1.08	1.96	0.00	3.04	−0.04	3.04
	Ti 1	2.13	6.62	2.61	11.35	0.65	3.35
	Ti 2	2.17	6.75	2.65	11.58	0.42	3.58

[a] Reference [20].
[b] Reference [29].

$$H_V = \left[\Pi^{\mu}\left(H_v^{\mu}\right)^{n^{\mu}}\right]^{1/\sum n^{\mu}} \quad (6)$$

where, n^{μ} is the number of bonds of μ-type comprising the actual multiband crystal.

Upon completion of the theoretical calculations, the Vickers hardness values of Zr_3PbC_2 and Hf_3PbC_2 compounds are determined to be 3.33 GPa and 4.42 GPa, respectively (Table 4). Hadi et al. [42] conducted analogous calculations for Zr_3SnC_2 and Hf_3SnC_2 compounds, revealing respective theoretical Vickers hardness values of 4.2 GPa and 4.7 GPa. Roknuzzaman et al. [20] reported a Vickers hardness of 4.9 GPa for Hf_3AlC_2, while Lapauw et al. [81] synthesized Zr_3AlC_2 and ascertained its Vickers hardness to be 4.4 GPa. Through this comparative analysis, we can infer that our investigated compounds exhibit slightly lower hardness values than other MAX phase compounds, making them more machinable. Notably, MAX phase materials are typically soft, with Vickers hardness values falling within the 2–8 GPa range [82].

The Vickers hardness is also lower for Zr-based phases than the Hf-based ones, like elastic constants and moduli. This can be explained with the help of the total DOS of the compounds presented herein Fig. 6. The peak position in the DOS measures the strength of the hybridized states; a hybridized peak in the lower position indicates a stronger bonding among the states. As evident, the positions of the peaks are lower for Zr_3PbC_2 compared to Hf_3PbC_2, indicating comparatively lower bonding strength of hybridized states; consequently, lower elastic moduli and hardness are observed for Zr_3PbC_2 compared to Hf_3PbC_2. A similar report has been noted for other MAX phases [83–85].

3.3.3. Elastic anisotropy

Elastic anisotropy, commonly known as the anisotropy parameter, describes how a material's elastic response to an external force changes with direction. In other words, it measures the degree to which the mechanical characteristics of a material, such as stiffness or Young's modulus, depend on the direction of load application. Elastic anisotropy can affect the kinetics and direction of phase transitions in materials, like the change from one crystal structure to another. Several physical and mechanical features, including unusual *bcc* slip, phase alterations, dislocation dynamics, precipitation, anisotropic deformation caused by plasticity, mechanical yield points, rupture behavior, friction within the material, elastic instability, and intense investigations of ab initio calculations, are significantly influenced by elastic anisotropy [86]. Firmly, the equations we have given below are used for determining shear Anisotropic factors A_1, A_2, and A_3; these three factors represent three

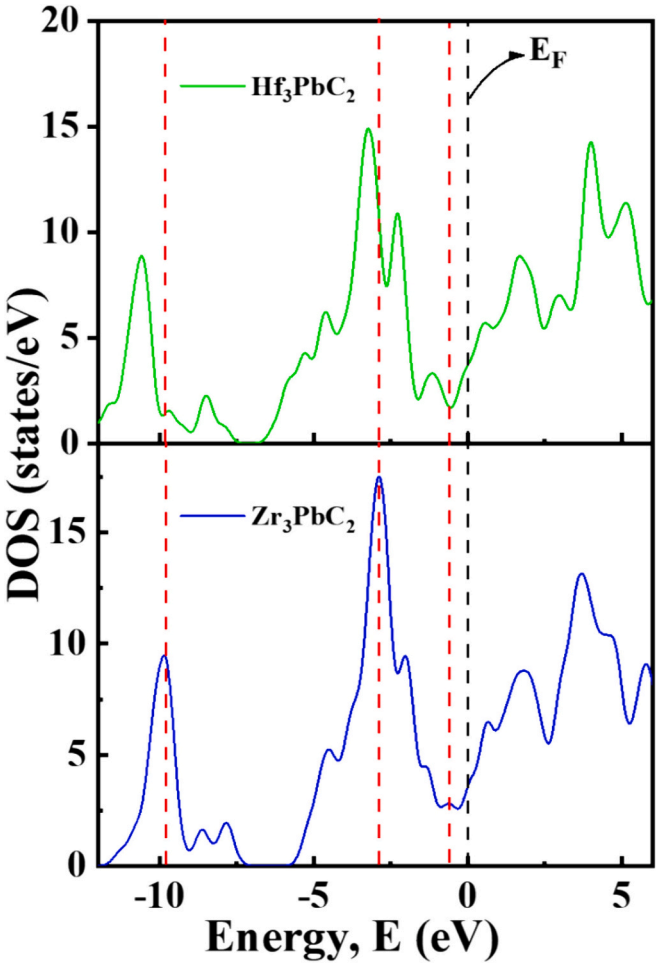

Fig. 6. Graphical view of the Total DOS for Zr_3PbC_2 and Hf_3PbC_2.

Table 4
Data for Mulliken bond number (n^{μ}), bond length (d^{μ}), bond overlap populations (P^{μ}), metallic populations ($P^{\mu'}$), Vickers hardness (H_V) of M_3PbC_2 (M = Zr, Hf) compounds.

Compound	Bond	n^{μ}	d^{μ} (Å)	P^{μ}	$P^{\mu'}$	v_b^{μ} (Å^3)	H_V^{μ} (GPa)	H_V (GPa)
Zr_3PbC_2	C-Zr1	4	2.267	1.25	0.0414	23.058	4.788	3.33
	C-Zr2	4	2.407	0.83		27.597	2.316	
Hf_3PbC_2	C-Hf1	4	2.278	1.65	0.0143	23.17	6.43	4.42
	C-Hf2	4	2.399	1.02		27.07	3.05	
Zr_3SnC_2[a]	Zr1-C	4	2.2697	1.24	0.00935	22.61	5.04	4.42
	Zr2-C	4	2.3973	0.88		26.64	3.56	
Hf_3AlC_2[b]	Hf-C	4	2.27173	1.46	0.0716	10.6137	20.044	4.9
	Hf-C	4	2.38140	1.02		15.6203	7.1904	
	Hf-Al	4	3.00404	0.78		47.327	0.8466	
Ti_3AlC_2[c]	Ti-C	4	2.07550	1.16	0.07208	7.75556	26.49355	8.96
	Ti-C	4	2.19815	0.88		9.21334	14.76516	
	Ti-Al	4	2.90778	0.48		21.3269	1.84045	
Ti_3SiC2[d]	Ti-C	4	2.09078	1.11	0.0131	8.40	23.39	10.89
	Ti-C	4	2.18730	0.89		9.62	14.92	
	Ti-Si	4	2.70384	0.64		18.172	3.70	

[a] Reference [42].
[b] Reference [20].
[c] Reference [4].
[d] Reference [29].

distinct elastic shear constants along the [100], [010] and [001] axes of a hexagonal crystal [86].

$$A_1 = \frac{\frac{1}{6}(C_{11}+C_{12}+2C_{33}-4C_{13})}{C_{44}}; A_2 = \frac{2C_{44}}{C_{11}-C_{12}}; A_3 = A_1 A_2 = \frac{\frac{1}{3}(C_{11}+C_{12}+2C_{33}-4C_{13})}{C_{11}-C_{12}} \quad (7)$$

The values given in Table 5 suggest that both compounds are anisotropic and as they are distinct from unity. Utilizing precise formulas, the linear compressibility anisotropy index (k_c/k_a) assesses the degree of compressibility along the *c*- and *a*-axes.

$$\frac{K_c}{K_a} = \frac{C_{11}+C_{12}-2C_{13}}{C_{33}-C_{13}} \quad (8)$$

This index shown in Table 5 deviates from one, demonstrating that the studied compounds are more compressible in the *c*-direction than the *a*-direction. The bulk modulus (Voigt, Reuss) and shear modulus (Voigt, Reuss) were used to compute the degree of anisotropy in compressibility (A_B) and shear (A_G) using the formulae presented:

$$A_B = \frac{B_V - B_R}{B_V + B_R} \times 100\%; A_G = \frac{G_V - G_R}{G_V + G_R} \times 100\% \quad (9)$$

For determining the universal anisotropic index, A^U, we use the following relation [65]:

$$A^U = 5\frac{G_V}{G_R} + \frac{B_V}{B_R} - 6 \geq 0 \quad (10)$$

The obtained values A_B, A_G, and A^U are non-zero, meaning all the solids presented here are anisotropic.

3.4. Vibrational properties

The Phonon Dispersion Curve (PDC) of a substance gives knowledge about configurational steadiness and vibrational offering in the thermodynamic possessions. The phonon dispersion is calculated at the equilibrium volume for a novel sequence of MAX phases along high symmetry directions, as shown in Fig. 7. The absence of negative frequency in the Brillouin zone demonstrates the dynamic stability of the freshly discovered MAX phases. The existence of a crystal structure is critically dependent on its inherent strength. A total of 36 vibrational modes appear at the zone's center in the 12-atom conventional unit cell of the studied MAX phases. Three of the 36 modes in this collection are acoustic (green lines), while the other 33 are optical (black lines). Lower branches of the dispersion curves that match the acoustic branches (green lines) can be seen as a result of coordinated movements of lattice atoms that deviate from their equilibrium positions. Inside the crystal's Brillouin zone (BZ), the phonon dispersion curve (PDC) and phonon density of states (PHDOS) for the studied phases have been calculated. The linear-response DFPT approach [39] was used to make this computation, as described in reference and shown in Fig. 7. The optical branch occupies the top part of the PDC and is crucial in determining the optical properties of the compound. At the zone center (*G*), the frequencies for the transverse optical (TO) and longitudinal optical (LO) phonon modes are found to be 16 and 16.8 THz, respectively.

The calculated overall phonon density of states (PHDOS) is shown in Fig. 7. The rather regular behavior of the bands is what causes the PHDOS to have peaks. In contrast, the heights of the peaks within the (DOS) are reduced when both upward and downward-sloping bands are present. Examining the relationship between a peak and the flatness or sloping of the bands surrounding it will help anyone better understand this idea. The dispersion curve shows that the relevant bands have an almost constant energy. As we focus our attention on the lower bands, their upward-sloping characteristics help to explain why the comprehensive DOS's peaks are less prominent.

Table 5
Calculated data for different anisotropy parameters A_1, A_2, A_3, B_a, B_c, k_c/k_a, A_B, A_G, and the universal anisotropy index (A^U) of M_3PbC_2 (M = Zr, Hf) compounds.

Phases	A_1	A_2	A_3	k_c/k_a	A_B	A_G	A^U
Zr_3PbC_2	1.24	0.76	0.94	1.30	0.36	0.59	0.07
Hf_3PbC_2	1.23	0.89	1.09	1.47	0.68	0.60	0.07
Zr_3SnC_2[a]	0.833	1.17	0.98	1.18	0.13	0.35	0.038
Hf_3SnC_2[a]	0.915	1.02	0.935	1.09	0.043	0.06	0.007
Ti_3AlC_2[b]	1.026	0.871	0.8948	1.271	0.036	0.281	0.036
Ti_3SiC_2[b]	0.812	1.128	0.916	0.998	0.00003	0.320	0.032

[a] Reference [42].
[b] Reference [29].

3.5. Thermal properties

The material's thermodynamic properties at elevated temperatures and pressures hold significant scientific and technological importance, as they contribute to our ability to anticipate the material's performance and applications under such extreme conditions. To compute these thermodynamic properties accurately, a comprehensive understanding of the vibrational spectrum and a high level of precision are essential.

Using the derived phonon density of states and the quasi-harmonic approximation [87], we determined the thermodynamic potential functions for M_3PbC_2 (M = Zr, Hf) at zero pressure, including the Helmholtz free energy *F*, internal energy *E*, entropy *S*, and specific heat C_v. The *F*, *E*, *S*, and C_v have been determined via the following equations [88]:

$$F = 3nN_A K_B T \int_0^{\omega_{max}} ln\left\{2sinh\left(\frac{\hbar\omega}{2K_B T}\right)\right\} g(\omega) d\omega \quad (11)$$

$$E = 3nN_A \frac{\hbar}{2} \int_0^{\omega_{max}} \omega coth\left(\frac{\hbar\omega}{2K_B T}\right) g(\omega) d\omega \quad (12)$$

$$S = 3nN_A K_B \int_0^{\omega_{max}} \left[\frac{\hbar\omega}{2K_B T} coth\left(\frac{\hbar\omega}{2K_B T}\right) - ln\left\{2sinh\left(\frac{\hbar\omega}{2K_B T}\right)\right\}\right] g(\omega) d\omega \quad (13)$$

$$C_v = 9nN_A K_B \left(\frac{T}{\theta_D}\right) \int_0^{x_D} \frac{x^4}{(e^x - 1)^2} \quad (14)$$

here "*n*" signifies the number of atoms within a unit cell, "*N*" stands for Avogadro's number, "ω_{max}" is the cut-off phonon frequency, "ω" is the phonon frequency, and "k_B" signifies the Boltzmann constant. To ensure that $f(g(\omega))d\omega = 1$, we normalize the phonon density of states $g(\omega)$, so that $\int_0^{\omega_{max}} g(\omega)d\omega = 1$, making $g(\omega) = (1/3nN)\sum_{q,l}^{\omega_{max}} \delta(\omega - \omega(q,l))$; where the phonon wave vector *q* and the phonon mode l.

Fig. 8(a–d) showcases the computed Free Energy (*F*), Internal Energy (*E*), Entropy (*S*), and Heat Capacity at Constant Volume (C_v) across the temperature range of 0 to 1000 K. Fig. 8(a) illustrates the Helmholtz free energy (*F*) of M_3PbC_2 (M = Zr, Hf), which exhibits a gradual decline as the temperature increases. Free energy often follows a decreasing trend, and this negative direction is a consistent characteristic of any natural process. A system's entropy (S) influences the extent of the free energy decrease. Entropy increases with rising temperature because thermal agitation contributes to greater disorder within the system. This phenomenon is depicted in Fig. 8(c). The internal energy (*E*) displays a rising pattern with increasing temperature, which contrasts with the behavior of free energy, as demonstrated in Fig. 8(b). Specific heat plays a significant role in predicting the density of states, band structure, and lattice vibrations. Fig. 8 illustrates the influence of temperature on the specific heat at constant volume (C_v) for M_3PbC_2 (M = Zr, Hf). At lower

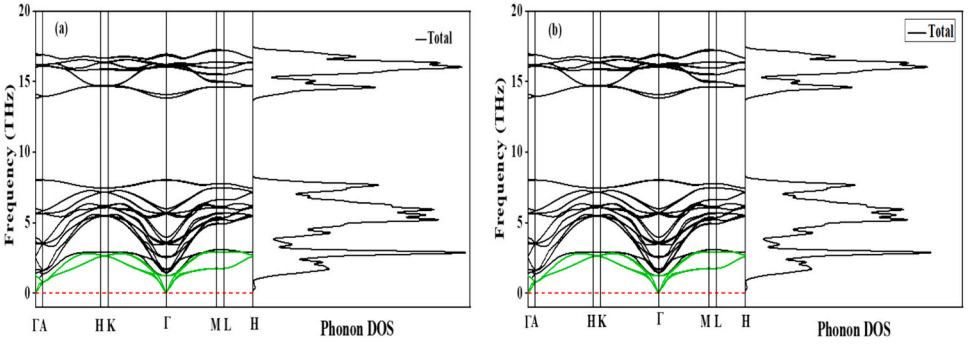

Fig. 7. Phonon dispersion and phonon DOS curves of (a) Hf_3PbC_2 (b) Zr_3PbC_2 compounds.

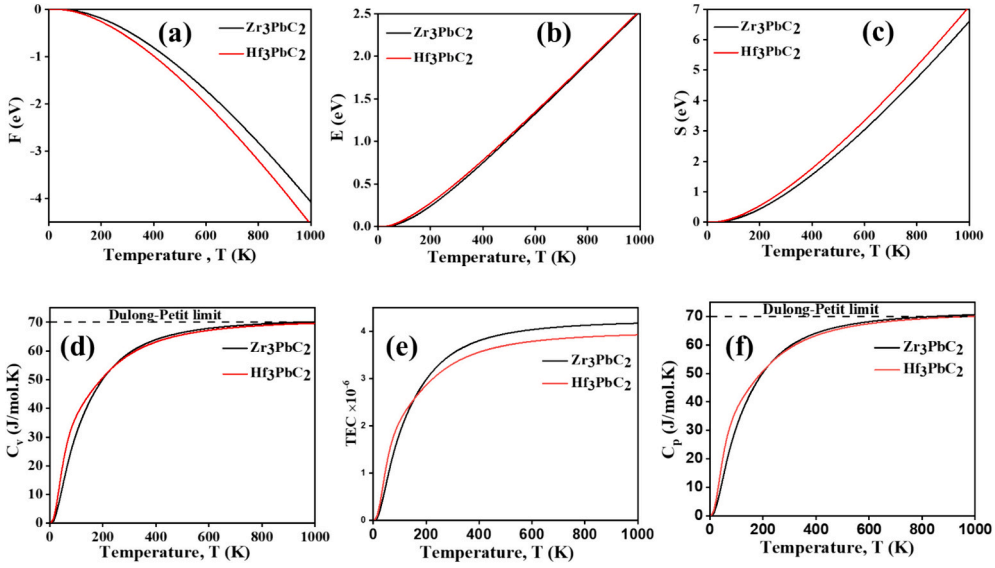

Fig. 8. The representation of (a) Helmholtz free energy (*F*), (b) internal energy (*E*), (c) entropy (*S*), (d, f) heat capacity at constant volume (C_v) and constant pressure (C_p), (e) thermal expansion coefficient (α) for M_3PbC_2 (M = Zr, Hf) compounds at different temperatures.

temperatures, the heat capacities of both MAX phases adhere to the Debye T^3 power-law, primarily because of the exponential increment in the number of excited phonon modes. Another thermal property, the linear thermal expansion coefficient (*TEC*), is related to the heat capacity at constant volume (C_v) and capacity at constant pressure expressed through the following equations [19].

$$TEC = \frac{\gamma Cv}{3B_T V_m}; C_p = C_v[1 + \alpha\gamma T] \tag{15}$$

where, γ, B_T V_m denote Grüneisen parameter, isothermal bulk modulus, and molar volume.

At temperatures above 600 *K*, the Dulong-Petit (DP) model is almost precisely followed. Furthermore, in Fig. 8(e), we show how temperature-dependent *TEC* varies. The results demonstrate that *TEC* proliferates up to 180 *K*, then steadily climbs between 200 *K* and 350 *K* before becoming nearly constant at high temperatures.

Understanding how heat is transferred at different temperature ranges is crucial when choosing a suitable Thermal Barrier Coating (TBC). As a result, both the minimum thermal conductivity (K_{min}) and the phonon thermal conductivity (K_{ph}) must be considered when investigating the application of M_3PbC_2 (M = Zr, Hf) as potential TBC materials. These characteristics rely on the Debye temperature (Θ_D) and the Grüneisen parameter (γ). The calculation is derived from the subsequent equation [89];

$$\Theta_D = \frac{h}{K_B}\left[\left(\frac{3n}{4\pi}\right)\frac{N_A\rho}{M}\right]^{\frac{1}{3}} v_m \tag{16}$$

Here, *M* represents the molecular weight, n stands for the number of atoms in the molecule, *r* is the mass density, and *h*, K_B, and N_A represent the Planck constant, Boltzmann constant, and Avogadro number, respectively. The mean sound velocity, denoted as V_m, is determined using the following formula:

$$v_m = \left[\frac{1}{3}\left(\frac{1}{v_l^3} + \frac{2}{v_t^3}\right)\right]^{-\frac{1}{3}} \tag{17}$$

Here, v_l and v_t represent the sound speeds in the longitudinal and transverse modes. These values, v_l and v_t, are computed using the subsequent equations [92]:

$$v_l = \left(\frac{3B + 4G}{3\rho}\right)^{\frac{1}{2}} \& v_t = \left(\frac{G}{\rho}\right)^{\frac{1}{2}} \tag{18}$$

Zr_3PbC_2 (~413 K) has a substantially higher value of Θ_D than the Hf-based compound Hf_3PbC_2 (~333 K), as also demonstrated by Hadi et al. (Zr_3SnC_2 ~ 480 K & Hf_3SnC_2 ~ 405 K) [42]. It is a result of Zr's lower atomic size. The Θ_D of the titled compounds, along with other 312 phases, is plotted in Fig. 9. Low Θ_D implies reduced thermal conductivity and compound stiffness. Materials with low heat conductivity show promise for TBC use. Table 6 reveals another significant factor: the

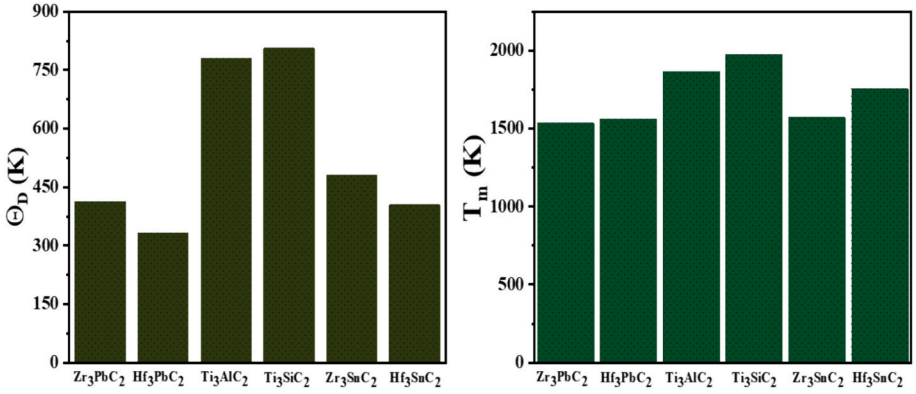

Fig. 9. Graphical view of the Θ_D (Left) and T_m (Right) of the studied compounds with previously worked compounds.

Table 6
Data for density (ρ in gm/cm^3), transverse, longitudinal and average sound velocities (v_l, v_t, v_m in m/s), Lattice thermal conductivity (K_{ph} in W/mK), Minimum thermal conductivity (K_{min} in W/mK), Grüneisen parameter (γ), Debye temperature (θ_D in K) and melting temperature of M_3PbC_2 (M = Zr and Hf) MAX phases.

Phases	ρ	v_t	v_l	v_m	Θ_D	K_{ph}	K_{min}	γ	T_m
Zr_3PbC_2	8.278	3210	5515	3561	413	14.31	0.75	1.5	1536
Hf_3PbC_2	12.674	2579	4522	2866	333	10.28	0.60	1.5	1563
Ti_3AlC_2[a]	4.2187[a]	5566.78[a]	8862.66[a]	6129.02[a]	780.7[a]	53.74[a]	1.550[a]	–	1866[a]
Ti_3SiC_2[a]	4.4907[a]	5631.31[a]	9124.48[a]	6211.83[a]	806.4[a]	52.12[a]	1.631[a]	–	1975[a]
Zr_3SnC_2[b]	7.019[b]	3756[b]	6316[b]	4818[b]	480[b]	–	–	–	1571[b]
Hf_3SnC_2[b]	11.526[b]	3117[b]	5247[b]	3452[b]	405[b]	–	–	–	1755[b]
Hf_3AlC_2[c]	10.29[c]	3514[c]	5675[c]	3874[c]	459[c]	–	–	–	–
$Y_4Al_2O_9$[d]	–	7020[d]	4000[d]	4450[d]	564[d]	–	1.12[d]	1.55[d]	–
Zr_2InB_2[e]	6.870[e]	6358[e]	3907[e]	4312[e]	516[e]	–	0.92[e]	1.28[e]	1693[e]

[a] Reference [29].
[b] Reference [42].
[c] Reference [20].
[d] Reference [90].
[e] Reference [91].

values of v_l are significantly larger than those of v_t. This means that the wave velocity in the transversal mode is lower than in the longitudinal mode because it takes extra energy to vibrate the nearby atoms [93].

In a computationally tractable manner, a metallic compound's lattice thermal conductivity (K_{ph}), such as MAX phases, gives an estimate of its total thermal conductivity. Motivated by these results, we computed the examined MAX phases' K_{ph}. For materials having dual characteristics (ceramic and metallic), such as MAX phases, the K_{ph} can be computed using the Slack model [94]. The K_{ph} can be computed using the equation that Slack deduced:

$$K_{ph} = A(\gamma)\frac{M_{av}{\Theta_D}^3\delta}{\gamma^2 n^{\frac{2}{3}}T}; \text{where}, \gamma = \frac{3(1+\upsilon)}{2(2-3\upsilon)}; \tag{19}$$

where δ is the cubic root of average atomic volume in meters, M_{av} states the average atomic mass in kg/mol, n represents the atom's number in a unit cell, Θ_D stands for the Debye temperature in K, T denotes the temperature in K, and γ signifies the Grüneisen parameter. The factor A (γ) stated by Julian [95] can be obtained as

$$A(\gamma) = \frac{4.85628 \times 10^7}{2\left(1 - \frac{0.514}{\gamma} + \frac{0.228}{\gamma^2}\right)} \tag{20}$$

Table 6 shows that the K_{ph} values for the phases under study are quite low, which suggests that the electronic contribution in terms of overall thermal conductivity at ambient temperature is higher than the lattice contribution for these compounds.

From the perspective of academic study and technical application, understanding anharmonic effects is crucial. The Grüneisen parameter (γ) measures a crystal's anharmonic effect [96]. An essential thermodynamics number, the Grüneisen parameter connects the bulk modulus, thermal expansion coefficient, heat capacity at constant volume, and volume collectively. Regarding polycrystalline elements, γ should be between 0.85 and 3.53, and the Poisson's ratio should be between 0.05 and 0.46 [97]. For high thermal conductivity materials, it was found that γ is low but higher for low thermal conductivity materials. This suggests that the compounds under investigation have higher anharmonic effects because we found higher values of γ (Table 6) [96]. Every solid has a minimum value of thermal conductivity at high temperatures, which is a property that is essential in deciding how solids are used in high temperatures. Phonons become unpaired at high temperatures and give heat energy to nearby atoms. Since there is not ever an optical mode in an individual "equivalent atom" in a cell, the minimum thermal conductivity (K_{min}) at excessive temperatures can be determined with Clarke's model [98] and the following formula:

$$K_{min} = K_B v_m \left(\frac{M}{n\rho N_A}\right)^{-\frac{2}{3}} \tag{21}$$

The Θ_D formula utilized in this research and the K_{min} formula used here both use the same symbols. Table 6 presents the calculated K_{min} values of 0.75 W/mK and 0.60 W/mK for the Zr_3PbC_2 and Hf_3PbC_2 compounds, respectively. The significantly reduced K_{min} values may be attributed to the higher Grüneisen parameter [96,99]. The observed low K_{min} values in the analyzed compounds lead to the anticipation that our investigated compound holds considerable potential for application as thermal barrier coating (TBC) material. In a study by Liu et al. [99], six perovskite compounds exhibited a K_{min} value of 1.25 W/m-K, suggesting their suitability as TBC materials. Let's delve into some intriguing TBC materials commonly employed in gas turbines, airplanes, and state-of-

the-art aero engines. The widely used Yttria-stabilized zirconia (7YSZ) boasts a K_{min} value of 2.2 (W/mK) [100]. Researchers have identified alternative TBC materials with high melting temperatures and low heat conductivity, such as $RE_2T_2O_7$ (RE = La, Pr, Nd, Sm, Eu, Gd, Y, Er, or Lu; T = Ti, Mo, Sn, Zr, or Pb), estimated to have K_{min} values ranging from 1.40 to 3.05 W/mK [100]. Rare earth stannates $RE_2Sn_2O_7$ (RE = La, Nd, Sm, Gd, Er, and Yb) exhibit K_{min} values from 1.8 to 2.5 W/mK. The perovskite oxides used for TBC applications are ABO_3 (A = Sr, Ba; B = Ti, Zr, Hf), with K_{min} values ranging from 1.09 to 1.74 W/mK [100]. Besides, the minimum thermal conductivities of certain pyrochlore oxides such as $La_2Ti_2O_7$, $La_2Ge_2O_7$, $La_2Zr_2O_7$, $La_2Sn_2O_7$, and $La_2Hf_2O_7$ have been examined. The respective minimum thermal conductivity values for these compounds are 1.17 W/m·K, 1.14 W/m·K, 1.03 W/m·K, 1.00 W/m·K, and 0.87 W/m·K. These values are relevant for applications in TBC [101]. These materials enhance thermal protection, ensure component longevity, and maintain performance in demanding operational conditions. Considering those above, it can be concluded that the K_{min} values of the Zr_3PbC_2 and Hf_3PbC_2 compounds are 0.75 W/mK and 0.60 W/mK, respectively, making them highly potential Thermal Barrier Coating (TBC) materials.

The formula proposed by Fine et al. have been used to compute the melting temperature (T_m) of the MAX phases from the stiffness constants such as C_{11} and C_{33} [64]:

$$T_m = 354 + 1.5(2C_{11} + C_{33}) \quad (22)$$

The calculated values of T_m are tabulated in Table 6 with some previous work data and plotted in Fig. 9. Certain zirconate compounds within the Pyrochlore family find application in higher temperature regions and exhibit superior thermal stability compared to the commonly utilized TBC material YSZ [102]. Specifically, zirconates involving Gd, La, Nd, and Sm possess a unique attribute in higher temperature regions, making them suitable as Electron Beam-Physical Vapor Deposition (EB-PVD) top coats within the temperature range of 973 K to 1473 K. Notably, the $Gd_2Zr_2O_7$ compound demonstrates thermal stability up to 1823 K [103]. Given this information, it is conceivable that the compounds under study may also be employed in higher-temperature environments.

3.6. Optical properties

This section examines the interactions of electromagnetic (EM) radiation with the studied materials. A substance's optical characteristics, which are crucial for optoelectronic applications, are related to the way that a substance reacts to an occurrence of electromagnetic radiation. Since the MAX phases have metallic properties, the optical properties of the metal and MAX phases are mostly determined by the electrons. Due to their shiny surfaces, metals and MAX phases exhibit high reflectivity and low light transmission, making MAX phases potential candidates for use as coating materials to lessen solar heating. They reflect light in the visible and infrared spectrums and up to a specific ultraviolet frequency known as the "plasma frequency," which has been mentioned in the "Loss function" section. The optical characteristics of the Zr_3PbC_2 and Hf_3PbC_2 compounds belonging to the 312 MAX phase have been calculated for energy up to 25 eV considering both (100) and (001) polarization direction, as illustrated in Fig. 10. Inter-band and intra-band transitions are well known to influence the dielectric properties of a metallic compound. Since the substances being studied are metallic, it is necessary to correct the low-energy region of the spectrum (intra-band). A semi-empirical Drude expression is employed to affect this alteration, characterized by a plasma frequency set at 3 eV, a Drude damping parameter of 0.05 eV, and a Gaussian smearing of 0.5 eV [20]. This action broadens the Fermi level, enhancing the impact of k-points on the Fermi surface. It is important to note that while the profiles for both polarization orientations are similar, they are not identical. The peak positions differ and can be distinguished by their respective intensities. When a material is exposed to sufficient energy light, electron

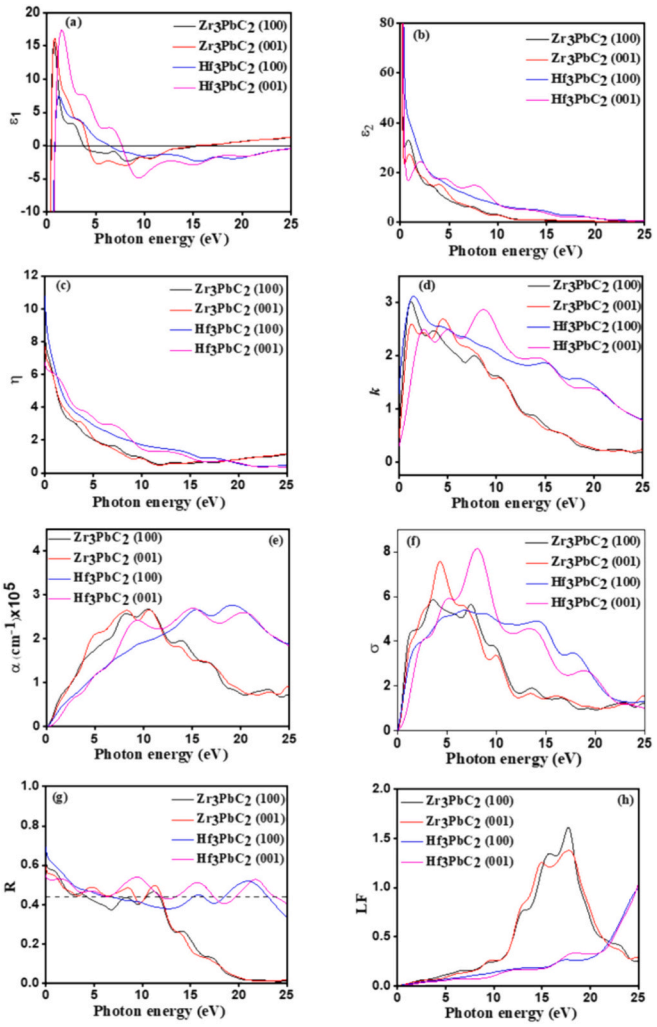

Fig. 10. (a) The real part $\varepsilon_1(\omega)$ (b) imaginary part $\varepsilon_2(\omega)$ of the dielectric function, (c) refractive index (η), (d) extinction coefficient (k), (e) absorption coefficient (α), (f) Photoconductivity (σ), (g) Reflectivity (R) and (h) loss function (LF).

transitions occur from occupied states below the Fermi level to unoccupied states above it. The dielectric constant represents a material's behavior in response to an applied electric field. Which is expressed by

$$\varepsilon(\omega) = \varepsilon_1(\omega) + i\varepsilon_2(\omega) \quad (23)$$

where the actual $\varepsilon_1(\omega)$ and the imaginary $\varepsilon_2(\omega)$ components adhere to the Kramers–Kronig relationships. It is established that the initial condition for computing the remaining optical constants necessitates the inclusion of the imaginary component $\varepsilon_2(\omega)$ in the dielectric function. The imaginary component of the dielectric constant is calculated using momentum matrix elements associated with occupied and unoccupied wave functions and selection rules. This can be stated as follows [104]:

$$\varepsilon_2(\omega) = \frac{2e^2\pi}{\Omega\varepsilon_0}\sum_{k,v,c}\left|\psi_k^c\right|u.r\left|\psi_k^v\right|^2\delta\left(E_k^c - E_k^v - E\right) \quad (24)$$

Within this equation, ω signifies the photon frequency, e represents the electronic charge, Ω stands for the volume of a unit cell, υ symbolizes the unit vector aligning with the polarization of the incoming electric field, and $\left|\psi_k^c\right|$ and $\left|\psi_k^v\right|$ respectively represents the wave functions of conduction and valence band electrons at a specific k point. The real component of the dielectric function can be obtained through the Kramers-Kronig transformation applied to the imaginary part [105].

$$\varepsilon_1(\omega) = 1 + \frac{2}{\pi} P \int_0^{\infty} \frac{\omega' \varepsilon_2(\omega') d\omega'}{(\omega'^2 - \omega^2)} \quad (25)$$

Fig. 10 illustrates the (a) real and (b) imaginary components of the complex dielectric function for M_3PbC_2(M═Zr, Hf). The dielectric function's real component, $\varepsilon_1(\omega)$, denotes the material's ability to store electrical energy (electronic polarizability) or to transmit an electric field. $\varepsilon_2(\omega)$ is related to dielectric loss, which is always positive, representing the loss factor or energy absorbed by a material within its unit volume. Within the low-energy range, the real component $\varepsilon_1(\omega)$ of the dielectric function is observed to cross zero from below, displaying negative values, and the imaginary component $\varepsilon_2(\omega)$ approaches zero from higher values. This observation indicates the metallic behavior of M_3PbC_2 (M = Zr, Hf). A similar pattern of $\varepsilon_1(\omega)$ and $\varepsilon_2(\omega)$ is also reported for Ti_2PB_2 and Zr_2PbB_2 [106] and Ti_3SiC_2 [107] MAX phases. The first peak in $\varepsilon_1(\omega)$ is observed in the 0.5 to 2.5 eV range, while the first peak is noticed at ~1.5 eV for Ti_3SiC_2. The peaks in $\varepsilon_2(\omega)$ indicate the intra or inter-band transition of electrons. For the present case, the peak in the low energy part is due to the intra-band transition within M-3*d* states.

The refractive index $\eta(\omega)$ of M_3PbC_2 (M = Zr, Hf), illustrated in Fig. 10(c), is a dimensionless quantity that indicates how much a medium can slow down the light. The substantial constant value in the range of 15–20 eV indicates the metallic behavior of the investigated MAX phases. A greater refractive index corresponds to a slower speed of light propagation through the medium, leading to increased light bending and more efficient refraction. Fig. 10(d) illustrates the imaginary component of the refractive index, also referred to as the extinction coefficient, $k(\omega)$. An exceptionally high value of $k(\omega)$ is attributed to a metallic substance, while an exceedingly low value of $k(\omega)$ is linked with a semiconductor material. Conversely, dielectric materials are primarily non-conductive and possess a $k(\omega)$ value of zero. For M_3PbC_2 (M = Zr, Hf), the constant range of $k(\omega)$ spans from 0.5 to 4.2 eV. Between 5 eV and 13 eV, the value of $k(\omega)$ surpasses $\eta(\omega)$, indicating an energy span where light cannot penetrate deeply into the compound [108]. This observation portrays the reflective metal attributes of M_3PbC_2 compounds.

$$n(\omega) = \frac{1}{\sqrt{2}} \left[\sqrt{\{\varepsilon_1(\omega)\}^2 + \{\varepsilon_2(\omega)\}^2} + \varepsilon_1(\omega) \right]^{1/2} \quad (26)$$

$$k(\omega) = \frac{1}{\sqrt{2}} \left[\sqrt{\{\varepsilon_1(\omega)\}^2 + \{\varepsilon_2(\omega)\}^2} - \varepsilon_1(\omega) \right]^{1/2} \quad (27)$$

$$\alpha(\omega) = \sqrt{2}\omega \left[\sqrt{\{\varepsilon_1(\omega)\}^2 + \{\varepsilon_2(\omega)\}^2} - \varepsilon_1(\omega) \right]^{1/2} \quad (28)$$

The absorption coefficient (α) in Fig. 10(e) represents the process by which matter (usually electrons confined in atoms) absorbs photon energy and converts it into internal energy of the absorber (such as thermal energy). It starts at 0 eV for {100} and {001} polarization direction. This indicates the metallic nature is evident from the beginning of their spectra, which commence at zero photon energy because of the absence of a bandgap. Furthermore, the peak values fall within the range of 2.2 to 2.6. Across nearly all instances and for both polarizations, the absorption spectra exhibit slight anisotropy throughout the entire range of photon energies.

The optical and electrical phenomenon known as photoconductivity occurs when a material absorbs electromagnetic rays, such as gamma, ultraviolet, visible light, or infrared rays, making it more electrically conductive. As depicted in Fig. 10(f), photoconductivity (σ) originates at zero photon energy due to the absence of a band gap in the materials, as evident from the band structure. The material's electrical conductivity increases due to photon absorption, contributing to its photoconductivity [109]. The Hf_3PbC_2 shows maximum photoconductivity at 8.13 eV for the (001) direction and 7.55 eV for Zr_3PbC_2 at the (001) direction.

$$\sigma(\omega) = \frac{\omega \varepsilon_2}{4\pi} \quad (29)$$

$$R(\omega) = \left| \frac{\sqrt{\varepsilon(\omega)} - 1}{\sqrt{\varepsilon(\omega)} + 1} \right|^2 \quad (30)$$

Fig. 10(g) exhibits the reflectivity (R) of the materials, which is a measure of the ability of a surface to reflect radiation, presented by the equation mentioned above [110–112]. As photon energy increases, there is a distinct reduction in reflectivity for Zr_3PbC_2 within the 13–30 eV range. Moreover, as the photon energy is further raised, there is a sharp alteration in reflectivity, reaching its apex between 35 and 42 eV at a value of 0.64. Regarding Hf_3PbC_2, the reflectivity experiences a nearly continuous decrease until it gets a minimum value of 0. The highest point for Hf_3PbC_2 is within the range of 18–24 eV, with the peak reflectivity recorded at 0.52. Li et al. [107] suggested that a material must have a reflectivity exceeding 44 % to qualify as a coating material. They identified Ti_4AlN_3 as such a material, with applications as a coating in spacecraft due to its ability to reflect 44 % of incident light. Our investigation observed a noteworthy result consistent with Li's findings. Zr_3PbC_2 and Hf_3PbC_2 compounds can reflect incident light up to 9.2 eV and 11.90 eV, respectively, for the (001) polarization direction. Moreover, Zr_3PbC_2 and Hf_3PbC_2 compounds demonstrate reflectivity >44 % up to 6.2 eV and 4.12 eV, respectively, for the (100) polarization direction. This phenomenon is reminiscent of observations in the UIr_3 intermetallic compound studied by Dujana et al. [113], where UIr_3 reflected 54 % of incident light up to an energy of 15 eV. Qureshi et al. [114] also completed a theoretical work on the Zr_3CdB_4 compound through the DFT method, and they suggested that Zr_3CdB_4 can be used as a coating material to diminish solar heating because it reflects 44 % of solar light. So, from the above comparison with other coating materials, we can easily suggest that our examined compounds are suitable for use as coating materials aimed at mitigating solar heating.

Fig. 10(h) shows the optical energy loss function $L(\omega)$. It describes how much a high-speed electron loses energy when it passes through a material and can be computed by the equation, $L(\omega) = \varepsilon_2(\omega)/\left[\{\varepsilon_1(\omega)\}^2 + \{\varepsilon_2(\omega)\}^2\right]$. It displays an opposite relationship with the imaginary part of the dielectric function. In Fig. 10(d), a wide peak exists in the imaginary part within the energy range of 0–5 eV, yet there isn't a noticeable prominent peak in the loss function. This suggests a high optical conductivity and minimal energy loss within this region. For Zr_3PbC_2, the notable peak emerges between 10 and 21 eV, while for Hf_3PbC_2, the peak appears in the 22–34 eV range. These peaks are consistent for both polarization planes. The bulk plasma frequency can be defined as the center of these peaks. The plasma frequency for Zr_3PbC_2 is 17.72 eV, while for Hf_3PbC_2, it is 29.72 eV. A comparable phenomenon is observed in the compound Hf_3PB_4, whose plasma frequency is 19 eV.

4. Environmental concerns of Pb-containing compounds

Since we concentrated on compounds containing lead, it is essential to discuss the toxic effects of lead on the environment. Pb is a kind of heavy nonferrous metal that resists corrosion. It is extensively utilized for radiation mitigation, cable, batteries, and the chemical industry. Pb is a metal with a greater bulk and atomic mass that is harmful to the environment as well as human health [115]. These hazardous metals are released into the environment in large quantities by several industries, including the pulp preservative, food, beverage, pharmaceutical, and newspaper industries. Mineral fertilizers made of coal contain a lot of heavy metals, like lead and mercury. All things considered, these uses are to blame for the increase in lead pollution in the environment [116].

The surrounding regions and local organisms are primarily impacted by these metal-based (Pb) pollutants when they are produced or released. Thus, some methods for the systematic disposal of pollutants

centered on site-specific Pb remediation are discussed by Raj et al. [117].

Despite having several adverse effects, Pb-containing compounds, as well as Pb-containing MAX phases, have been studied and have exceptional mechanical, thermal, and optical qualities and are used in high-temperature, nuclear, solar, and oxidation-resistant applications, among other areas. For example, Hossain et al. studied Hf_2AB (A = Pb, Bi) and found that the compounds can be used as a cover material [68]. Pb-containing 212 MAX phases were studied by Ali et al., and they explored that these compounds show excellent thermal properties, including an increment in Debye and melting temperatures [106]. Hussein et al. found the corrosion & oxidation resistance and self-healing behavior of Pb-containing MAX phases [118]. Srinivasan et al. found that Ti_2AN (A = TI, Pb) can be used as a TBC material as well as in many high temperature applications [119]. Moreover, the Pb-containing MAX phases are already synthesized successfully [120]. However, it is essential to note that the adverse effects of Pb-containing phases must be carefully considered before practical application, and precautions should be taken to minimize these adverse effects.

5. Conclusions

We conducted a DFT investigation to analyze the physical properties of newly synthesized Zr_3PbC_2 and Hf_3PbC_2 compounds. The lattice constants consent with the experimental data. The electronic band structure certifies the metallic nature of the studied compounds. According to the DOS figure, the Zr-4*d* and Hf-5*d* electrons are responsible for the electronic contribution at the Fermi level. The charge density mapping affirms the existence of a strong covalent bond between M and C atoms and a weaker covalent bond between Pb and C atoms within these compounds. Elastic constants demonstrated the mechanical stability of the studied compounds, and the brittleness is confirmed by Pugh's ratio and Poisson's ratio. The *f*-index value indicates that the studied compounds can be exfoliated into a 2D nanosheet (MXene). Low elastic moduli (*B*, *G*, and *Y*) and Vickers hardness values (3.33 GPa for Zr_3PbC_2 and 4.42 GPa for Hf_3PbC_2) confirmed their soft nature, which in turn certifies the excellent machinability of them. The existence of ionic bonding has been confirmed by the transfer of charge from the M atom to the Pb and/or C atoms. Anisotropic elastic properties have been confirmed, where Zr_3PbC_2 exhibits lower anisotropy indices compared to that of Hf_3PbC_2. Furthermore, the phonon dispersion curve assures the dynamical stability of the compounds. The vital thermal parameters such as low thermal expansion coefficient, high melting temperature (1536 K and 1563 K for Zr_3PbC_2 and Hf_3PbC_2), very low value of minimum thermal conductivity (0.75 W/mK and 0.60 W/mK for the Zr_3PbC_2 and Hf_3PbC_2) established them as potential TBC materials. Moreover, the preferable outcome of the optical property's analysis suggests that Zr_3PbC_2 and Hf_3PbC_2 could be potential candidates for coating materials to mitigate solar heating. Though the compounds have potential practical applications, their toxic effects must be considered, and precautions must be taken to minimize harm, such as proper waste disposal and shielding.

CRediT authorship contribution statement

M.R. Rana: Writing – original draft, Validation, Formal analysis. **S. Islam:** Writing – original draft, Validation, Formal analysis. **K. Hoque:** Writing – review & editing, Validation. **S. Mahmud:** Investigation, Data curation. **M.A. Ali:** Writing – review & editing, Validation, Supervision, Project administration, Methodology, Conceptualization.

Declaration of competing interest

The authors declare that they have no known competing financial interests or personal relationships that could have appeared to influence the work reported in this paper.

Data availability

Data will be made available on request.

Acknowledgments

This work was carried out in ACMRL, which was established with the aid of a grant (grant number: 21-378 RG/PHYS/AS_G-FR3240319526) from UNESCO-TWAS and the Swedish International Development Cooperation Agency (SIDA). The views expressed herein do not necessarily represent those of UNESCO-TWAS, SIDA or its Board of Governors.

References

[1] M.W. Barsoum, The $M_{N+1}AX_N$ phases: a new class of solids, Prog. Solid State Chem. 28 (1–4) (Jan. 2000) 201–281, https://doi.org/10.1016/S0079-6786(00)00006-6.

[2] M.W. Barsoum, T. El-Raghy, The MAX phases: unique new carbide and nitride materials: ternary ceramics turn out to be surprisingly soft and machinable, yet also heat-tolerant, strong and lightweight, Am. Sci. 89 (4) (2001) 334–343. Accessed: Oct. 17, 2023. [Online]. Available: http://www.jstor.org/stable/27857502.

[3] M.A. Hadi, S.-R.G. Christopoulos, A. Chroneos, S.H. Naqib, A.K.M.A. Islam, DFT insights into the electronic structure, mechanical behaviour, lattice dynamics and defect processes in the first Sc-based MAX phase Sc_2SnC, Sci. Rep. 12 (1) (Aug. 2022) 14037, https://doi.org/10.1038/s41598-022-18336-z.

[4] E. Zapata-Solvas, et al., Synthesis and physical properties of $(Zr_{1-x},Ti_x)_3AlC_2$ MAX phases, J. Am. Ceram. Soc. 100 (8) (Aug. 2017) 3393–3401, https://doi.org/10.1111/jace.14870.

[5] M.W. Barsoum, T. El-Raghy, Room-temperature ductile carbides, Metall. Mater. Trans. A 30 (2) (Feb. 1999) 363–369, https://doi.org/10.1007/s11661-999-0325-0.

[6] M.W. Barsoum, MAX Phases: Properties of Machinable Ternary Carbides and Nitrides, John Wiley & Sons, 2013.

[7] S. Hwang, S.C. Lee, J. Han, D. Lee, S.-W. Park, Machinability of Ti_3SiC_2 with layered structure synthesized by hot pressing mixture of TiCx and Si powder, J. Eur. Ceram. Soc. 32 (12) (Sep. 2012) 3493–3500, https://doi.org/10.1016/j.jeurceramsoc.2012.04.021.

[8] T. El-Raghy, A. Zavaliangos, M.W. Barsoum, S.R. Kalidindi, Damage mechanisms around hardness indentations in Ti_3SiC_2, J. Am. Ceram. Soc. 80 (2) (Feb. 1997) 513–516, https://doi.org/10.1111/j.1151-2916.1997.tb02861.x.

[9] B.J. Kooi, R.J. Poppen, N.J.M. Carvalho, J.T.M. De Hosson, M.W. Barsoum, Ti3SiC2: a damage tolerant ceramic studied with nano-indentations and transmission electron microscopy, Acta Mater. 51 (10) (Jun. 2003) 2859–2872, https://doi.org/10.1016/S1359-6454(03)00091-0.

[10] M.N. Uddin, A.K.M.N. Ishtiaq, S. Islam, M.R. Rana, M.A. Ali, K. Hoque, Prediction of new 212 M_2AB_2 borides as a promising candidate for future engineering: DFT calculations, Mater. Today Commun. 39 (January) (Jun. 2024) 108536, https://doi.org/10.1016/j.mtcomm.2024.108536.

[11] D.J. Tallman, L. He, J. Gan, E.N. Caspi, E.N. Hoffman, M.W. Barsoum, Effects of neutron irradiation of Ti_3SiC_2 and Ti_3AlC_2 in the 121–1085 °C temperature range, J. Nucl. Mater. 484 (Feb. 2017) 120–134, https://doi.org/10.1016/j.jnucmat.2016.11.016.

[12] Q. Huang, et al., Irradiation resistance of MAX phases Ti_3SiC_2 and Ti_3AlC_2: characterization and comparison, J. Nucl. Mater. 465 (Oct. 2015) 640–647, https://doi.org/10.1016/j.jnucmat.2015.06.056.

[13] C. Magnus, J. Sharp, W.M. Rainforth, The lubricating properties of spark plasma sintered (SPS) Ti_3SiC_2 MAX phase compound and composite, Tribol. Trans. 63 (1) (Jan. 2020) 38–51, https://doi.org/10.1080/10402004.2019.1657534.

[14] M. Naguib, et al., Two-dimensional nanocrystals produced by exfoliation of Ti_3AlC_2, Adv. Mater. 23 (37) (Oct. 2011) 4248–4253, https://doi.org/10.1002/adma.201102306.

[15] M.W. Barsoum, T. El-Raghy, Synthesis and characterization of a remarkable ceramic: Ti_3SiC_2, J. Am. Ceram. Soc. 79 (7) (Jul. 1996) 1953–1956, https://doi.org/10.1111/j.1151-2916.1996.tb08018.x.

[16] C.M. Fang, R. Ahuja, O. Eriksson, Prediction of MAX phases, $V_{N+1}SiC_N$ (N=1,2), from first-principles theory, J. Appl. Phys. 101 (1) (Jan. 2007) 3–6, https://doi.org/10.1063/1.2405721.

[17] D.T. Cuskelly, E.R. Richards, E.H. Kisi, V.J. Keast, Ti_3GaC_2 and Ti_3InC_2: first bulk synthesis, DFT stability calculations and structural systematics, J. Solid State Chem. 230 (Oct. 2015) 418–425, https://doi.org/10.1016/j.jssc.2015.07.028.

[18] X. He, Y. Bai, Y. Chen, C. Zhu, M. Li, M.W. Barsoum, Phase stability, electronic structure, compressibility, elastic and optical properties of a newly discovered Ti_3SnC_2: a first-principle study, J. Am. Ceram. Soc. 94 (11) (Nov. 2011) 3907–3914, https://doi.org/10.1111/j.1551-2916.2011.04593.x.

[19] M.A. Rayhan, M.A. Ali, S.H. Naqib, A.K.M.A. Islam, First-principles study of Vickers hardness and thermodynamic properties of Ti_3SnC_2 polymorphs, J. Sci. Res. 7 (3) (Sep. 2015) 53–64, https://doi.org/10.3329/jsr.v7i3.23182.

[20] M. Roknuzzaman, et al., First hafnium-based MAX phase in the 312 family, Hf_3AlC_2: a first-principles study, J. Alloys Compd. 727 (Dec. 2017) 616–626, https://doi.org/10.1016/j.jallcom.2017.08.151.

[21] H. Fashandi, et al., Synthesis of Ti_3AuC_2, $Ti_3Au_2C_2$ and Ti_3IrC_2 by noble metal substitution reaction in Ti_3SiC_2 for high-temperature-stable Ohmic contacts to SiC, Nat. Mater. 16 (8) (Aug. 2017) 814–818, https://doi.org/10.1038/nmat4896.

[22] L. Chen, G. Duan, X.F. Gao, C.L. Wang, Property of mono-vacancy in MAX phase M_3AC_2 (M=Ti, A=Al, Si, or Ge): first-principles calculations, Mod. Phys. Lett. B 32 (15) (May 2018) 1850160, https://doi.org/10.1142/S0217984918501609.

[23] I. Ouadha, H. Rached, A. Azzouz-Rached, A. Reggad, D. Rached, Study of the structural, mechanical and thermodynamic properties of the new MAX phase compounds $(Zr_{1-x}Ti_x)_3AlC_2$, Comput. Condens. Matter 23 (2020), https://doi.org/10.1016/j.cocom.2020.e00468.

[24] A. Azzouz-Rached, M.A. Hadi, H. Rached, T. Hadji, D. Rached, A. Bouhemadou, Pressure effects on the structural, elastic, magnetic and thermodynamic properties of Mn_2AlC and Mn_2SiC MAX phases, J. Alloys Compd. 885 (SPEC. ISS) (Dec. 2021) 160998, https://doi.org/10.1016/j.jallcom.2021.160998.

[25] A. Azzouz-Rached, H. Rached, I. Ouadha, D. Rached, A. Reggad, The Vanadium-doping effect on physical properties of the Zr_2AlC MAX phase compound, Mater. Chem. Phys. 260 (December 2020) (Feb. 2021) 124189, https://doi.org/10.1016/j.matchemphys.2020.124189.

[26] A. Azzouz-Rached, M.M. Haque Babu, H. Rached, T. Hadji, D. Rached, Prediction of a new Sn-based MAX phases for nuclear industry applications: DFT calculations, Mater. Today Commun. 27 (March) (Jun. 2021) 102233, https://doi.org/10.1016/j.mtcomm.2021.102233.

[27] A. Azzouz-Rached, M. Waqas Qureshi, I. Ouadha, H. Rached, T. Hadji, H. Rekab-Djabri, DFT analysis of physical properties of quaternary MAX phase nitrides: $(Fe_{0.5}M_{0.5})_2SiN$ (M = Cr & Mn), Comput. Condens. Matter 33 (July) (2022), https://doi.org/10.1016/j.cocom.2022.e00748.

[28] A.A. Belkacem, et al., The stability analysis and efficiency of the new MAX-phase compounds M_3GaC_2 (M: Ti or Zr): a first-principles assessment, Results Phys. 38 (May) (Jul. 2022) 105621, https://doi.org/10.1016/j.rinp.2022.105621.

[29] M.A. Hadi, et al., A comparative DFT exploration on M- and A-site double transition metal MAX phase, Ti_3ZnC_2, Open Ceram. 12 (September) (Dec. 2022) 100308, https://doi.org/10.1016/j.oceram.2022.100308.

[30] M.A. Hadi, N. Kelaidis, S.-R.G. Christopoulos, A. Chroneos, S.H. Naqib, A.K.M. A. Islam, Optical response, lithium doping, and charge transfer in Sn-based 312 MAX phases, ACS Omega 8 (28) (Jul. 2023) 25601–25609, https://doi.org/10.1021/acsomega.3c03645.

[31] Q. Zhang, et al., Synthesiscv of new lead-containing MAX phases of Zr_3PbC_2 and Hf_3PbC_2, J. Am. Ceram. Soc. 106 (11) (Nov. 2023) 6390–6397, https://doi.org/10.1111/jace.19332.

[32] M.D. Segall, et al., First-principles simulation: ideas, illustrations and the CASTEP code, J. Phys. Condens. Matter 14 (11) (Mar. 2002) 2717–2744, https://doi.org/10.1088/0953-8984/14/11/301.

[33] D.C. Langreth, M.J. Mehl, Beyond the local-density approximation in calculations of ground-state electronic properties, Phys. Rev. B 28 (4) (1983) 1809–1834, https://doi.org/10.1103/PhysRevB.28.1809.

[34] J.P. Perdew, K. Burke, M. Ernzerhof, Generalized gradient approximation made simple, Phys. Rev. Lett. 77 (18) (1996) 3865–3868, https://doi.org/10.1103/PhysRevLett.77.3865.

[35] A.D. Becke, Density-functional exchange-energy approximation with correct asymptotic behavior, Phys. Rev. A 38 (6) (Sep. 1988) 3098–3100, https://doi.org/10.1103/PhysRevA.38.3098.

[36] D. Vanderbilt, Rapid Communications vol. 41, no. 11, 1990, pp. 7892–7895.

[37] J.D. Pack, H.J. Monkhorst, 'Special points for Brillouin-zone integrations'-a reply, Phys. Rev. B 16 (4) (1977) 1748–1749, https://doi.org/10.1103/PhysRevB.16.1748.

[38] T.H. Fischer, J. Almlöf, General methods for geometry and wave function optimization, J. Phys. Chem. 96 (24) (1992) 9768–9774, https://doi.org/10.1021/j100203a036.

[39] K. Refson, P.R. Tulip, S.J. Clark, Variational density-functional perturbation theory for dielectrics and lattice dynamics, Phys. Rev. B - Condens. Matter Mater. Phys. 73 (15) (2006) 1–12, https://doi.org/10.1103/PhysRevB.73.155114.

[40] P.P. Filippatos, et al., 312 MAX phases: elastic properties and lithiation, Materials (Basel) 12 (24) (2019) 1–13, https://doi.org/10.3390/MA12244098.

[41] M.W. Qureshi, X. Ma, G. Tang, R. Paudel, Ab initio predictions of structure and physical properties of the Zr_2GaC and Hf_2GaC MAX phases under pressure, Sci. Rep. 11 (1) (2021) 1–23, https://doi.org/10.1038/s41598-021-82402-1.

[42] M.A. Hadi, S.-R.G. Christopoulos, S.H. Naqib, A. Chroneos, M.E. Fitzpatrick, A.K. M.A. Islam, Physical properties and defect processes of M_3SnC_2 (M = Ti, Zr, Hf) MAX phases: effect of M-elements, J. Alloys Compd. 748 (Jun. 2018) 804–813, https://doi.org/10.1016/j.jallcom.2018.03.182.

[43] W. Zhou, B. Mei, J. Zhu, Fabrication of high-purity ternary carbide Ti_3AlC_2 by spark plasma sintering (SPS) technique, Ceram. Int. 33 (7) (Sep. 2007) 1399–1402, https://doi.org/10.1016/j.ceramint.2006.04.018.

[44] Y. Zhou, Z. Sun, Electronic structure and bonding properties of layered machinable and ceramics, Phys. Rev. B - Condens. Matter Mater. Phys. 61 (19) (2000) 12570–12573, https://doi.org/10.1103/PhysRevB.61.12570.

[45] C.D. Gelatt, A.R. Williams, V.L. Moruzzi, Theory of bonding of transition metals to nontransition metals, Phys. Rev. B 27 (4) (Feb. 1983) 2005–2013, https://doi.org/10.1103/PhysRevB.27.2005.

[46] M.W. Barsoum, et al., Thermal and electrical properties of Nb_2AlC, $(Ti, Nb)_2AlC$ and Ti_2AlC, Metall. Mater. Trans. A Phys. Metall. Mater. Sci. 33 (9) (2002) 2775–2779, https://doi.org/10.1007/s11661-002-0262-7.

[47] M.W. Barsoum, J. Golczewski, H.J. Seifert, F. Aldinger, Fabrication and electrical and thermal properties of Ti_2InC, Hf_2InC and $(Ti,Hf)_2InC$, J. Alloys Compd. 340 (1–2) (Jun. 2002) 173–179, https://doi.org/10.1016/S0925-8388(02)00107-X.

[48] M.W. Barsoum, M. Ali, T. El-Raghy, Processing and characterization of Ti_2AlC, Ti_2AlN, and $Ti_2AlC_{0.5}N_{0.5}$, Metall. Mater. Trans. A Phys. Metall. Mater. Sci. 31 (7) (2000) 1857–1865, https://doi.org/10.1007/s11661-006-0243-3.

[49] L. Qu, et al., Synthesis, crystal structure, microstructure and mechanical properties of $(Ti1\text{-}Zr)_3SiC_2$ MAX phase solid solutions, Ceram. Int. 45 (1) (Jan. 2019) 1400–1408, https://doi.org/10.1016/j.ceramint.2018.10.030.

[50] M. Rühle, F. Ernst, High-Resolution Imaging and Spectrometry of Materials, Springer Verlag, 2003.

[51] P. Eklund, M. Beckers, U. Jansson, H. Högberg, L. Hultman, Linköping University post print the $M_{n+1}AX_n$ phases: materials science and thin-film processing, Mater. Sci. Thin-Film Process. 518 (2010) 1851–1878, https://doi.org/10.1016/j.tsf.2009.07.184.

[52] V.H. Nowotny, Strukturchemie einiger Verbindungen der Übergangsmetalle mit den elementen C, Si, Ge, Sn, Prog. Solid State Chem. 5 (C) (1971) 27–70, https://doi.org/10.1016/0079-6786(71)90016-1.

[53] F. Mouhat, F.X. Coudert, Necessary and sufficient elastic stability conditions in various crystal systems, Phys. Rev. B - Condens. Matter Mater. Phys. 90 (22) (2014) 4–7, https://doi.org/10.1103/PhysRevB.90.224104.

[54] A. Reuss, A. reuss, z. angew. math. mech. 9, 49 (1929), Z. Angew. Math. Mech. 9 (1929) 49.

[55] W. Voigt, Lehrbuch der Kristallphysik, Lehrbuch der Kristallphysik, Teubner, Leipzig, 1928.

[56] R. Hill, The elastic behaviour of a crystalline aggregate, Proc. Phys. Soc. Sect. A 65 (5) (1952) 349–354, https://doi.org/10.1088/0370-1298/65/5/307.

[57] W. Son, T. Duong, A. Talapatra, H. Gao, R. Arróyave, M. Radovic, Ab-initio investigation of the finite-temperatures structural, elastic, and thermodynamic properties of Ti_3AlC_2 and Ti_3SiC_2, Comput. Mater. Sci. 124 (Nov. 2016) 420–427, https://doi.org/10.1016/j.commatsci.2016.08.015.

[58] X. He, Y. Bai, C. Zhu, Y. Sun, M. Li, M.W. Barsoum, General trends in the structural, electronic and elastic properties of the M_3AlC_2 phases (M = transition metal): a first-principle study, Comput. Mater. Sci. 49 (3) (2010) 691–698, https://doi.org/10.1016/j.commatsci.2010.06.012.

[59] A. Champagne, et al., Insights into the elastic properties of RE- i -MAX phases and their potential exfoliation into two-dimensional RE- i -MXenes, Phys. Rev. Mater. 4 (1) (2020) 13604, https://doi.org/10.1103/PhysRevMaterials.4.013604.

[60] Z. Sun, D. Music, R. Ahuja, J.M. Schneider, Theoretical investigation of the bonding and elastic properties of nanolayered ternary nitrides, Phys. Rev. B - Condens. Matter Mater. Phys. 71 (19) (2005) 3–5, https://doi.org/10.1103/PhysRevB.71.193402.

[61] I.N. Frantsevich, Elastic Constants and Elastic Moduli of Metals and Insulators, Naukova Dumka, 1982.

[62] O.L. Anderson, H.H. Demarest, Elastic constants of the central force model for cubic structures: polycrystalline aggregates and instabilities, J. Geophys. Res. 76 (5) (1971) 1349–1369, https://doi.org/10.1029/jb076i005p01349.

[63] A. Savin, H.-J. Flad, J. Flad, H. Preuss, H.G. von Schnering, On the bonding in carbosilanes, Angew. Chemie Int. Ed. English 31 (2) (1992) 185–187, https://doi.org/10.1002/anie.199201851.

[64] S. Islam, et al., A comprehensive exploration of the physical properties of M_2GaB (M = Ti, Zr, Mo, Hf) through DFT method, Results Mater. 19 (April) (Sep. 2023) 100438, https://doi.org/10.1016/j.rinma.2023.100438.

[65] M.R. Rana, et al., DFT prediction of the stability and physical properties of M_2GaB (M = Sc, V, Nb, Ta), J. Mater. Res. Technol. 24 (May 2023) 7795–7815, https://doi.org/10.1016/j.jmrt.2023.05.008.

[66] X.-Q. Chen, H. Niu, D. Li, Y. Li, Modeling hardness of polycrystalline materials and bulk metallic glasses, Intermetallics 19 (9) (Sep. 2011) 1275–1281, https://doi.org/10.1016/j.intermet.2011.03.026.

[67] C. Zuo, C. Zhong, Screen the elastic and thermodynamic properties of MAX solid solution using DFT procedue: case study on $(Ti_{1-x}V_x)_2AlC$, Mater. Chem. Phys. 250 (April) (Aug. 2020) 123059, https://doi.org/10.1016/j.matchemphys.2020.123059.

[68] M.S. Hossain, M.A. Ali, M.M. Hossain, M.M. Uddin, Physical properties of predicted MAX phase borides Hf_2AB (A = Pb, Bi): a DFT insight, Mater. Today Commun. 27 (Jun. 2021) 102411, https://doi.org/10.1016/j.mtcomm.2021.102411.

[69] M.M. Hossain, et al., Influence of Se doping on recently synthesized $NaInS_{2-x}Se_x$ solid solutions for potential thermo-mechanical applications studied via first-principles method, Mater. Today Commun. 26 (August 2020) (2021) 101988, https://doi.org/10.1016/j.mtcomm.2020.101988.

[70] A. Yang, Y. Duan, L. Bao, M. Peng, L. Shen, Elastic properties, tensile strength, damage tolerance, electronic and thermal properties of TM_3AlC_2 (TM = Ti, Zr and Hf) MAX phases: a first-principles study, Vacuum 206 (Dec. 2022) 111497, https://doi.org/10.1016/j.vacuum.2022.111497.

[71] Y. Wang, M.X. Li, H.L. Suo, Mechanical properties of YSZ thermal barrier coatings with segmented structure, Surf. Eng. 28 (5) (Jun. 2012) 329–332, https://doi.org/10.1179/1743294412Y.0000000006.

[72] I.R. Shein, A.L. Ivanovskii, Elastic properties of superconducting MAX phases from first-principles calculations, Phys. Status Solidi Basic Res. 248 (1) (2011) 228–232, https://doi.org/10.1002/pssb.201046163.

[73] R.S. Mulliken, Electronic population analysis on LCAO–MO molecular wave functions. II. Overlap populations, bond orders, and covalent bond energies, J. Chem. Phys. 23 (10) (Oct. 1955) 1841–1846, https://doi.org/10.1063/1.1740589.

[74] M.A. Hadi, S.H. Naqib, S.-R.G. Christopoulos, A. Chroneos, A.K.M.A. Islam, Mechanical behavior, bonding nature and defect processes of Mo_2ScAlC_2: a new ordered MAX phase, J. Alloys Compd. 724 (Nov. 2017) 1167–1175, https://doi.org/10.1016/j.jallcom.2017.07.110.

[75] D. Sanchez-Portal, E. Artacho, J.M. Soler, Projection of plane-wave calculations into atomic orbitals, Solid State Commun. 95 (10) (Sep. 1995) 685–690, https://doi.org/10.1016/0038-1098(95)00341-X.

[76] M.A. Ali, M.A. Hadi, M.M. Hossain, S.H. Naqib, A.K.M.A. Islam, Theoretical investigation of structural, elastic, and electronic properties of ternary boride MoAlB, Phys. Status Solidi 254 (7) (Jul. 2017), https://doi.org/10.1002/pssb.201700010.

[77] E. Zapata-Solvas, et al., Synthesis and physical properties of $(Zr_{1-x}, Ti_x)_3AlC_2$ MAX phases, J. Am. Ceram. Soc. 100 (8) (Aug. 2017) 3393–3401, https://doi.org/10.1111/jace.14870.

[78] F. Gao, Theoretical model of intrinsic hardness, Phys. Rev. B 73 (13) (Apr. 2006) 132104, https://doi.org/10.1103/PhysRevB.73.132104.

[79] H. Gou, L. Hou, J. Zhang, F. Gao, Pressure-induced incompressibility of ReC and effect of metallic bonding on its hardness, Appl. Phys. Lett. 92 (24) (Jun. 2008) 0–3, https://doi.org/10.1063/1.2938031.

[80] M.T. Nasir, et al., First-principles study of superconducting ScRhP and ScIrP pnictides, Phys. Status Solidi 254 (11) (Nov. 2017) 1–10, https://doi.org/10.1002/pssb.201700336.

[81] T. Lapauw, et al., Synthesis of the novel Zr_3AlC_2 MAX phase, J. Eur. Ceram. Soc. 36 (3) (Feb. 2016) 943–947, https://doi.org/10.1016/j.jeurceramsoc.2015.10.011.

[82] M. Sokol, V. Natu, S. Kota, M.W. Barsoum, On the chemical diversity of the MAX phases, Trends Chem. 1 (2) (May 2019) 210–223, https://doi.org/10.1016/j.trechm.2019.02.016.

[83] M.A. Ali, M.M. Hossain, M.M. Uddin, M.A. Hossain, A.K.M.A. Islam, S.H. Naqib, Physical properties of new MAX phase borides M_2SB (M = Zr, Hf and Nb) in comparison with conventional MAX phase carbides M_2SC (M = Zr, Hf and Nb): comprehensive insights, J. Mater. Res. Technol. 11 (Mar. 2021) 1000–1018, https://doi.org/10.1016/j.jmrt.2021.01.068.

[84] M.A. Ali, et al., Recently synthesized $(Zr_{1-x}\ Ti_x)_2AlC$ ($0 \leq x \leq 1$) solid solutions: theoretical study of the effects of M mixing on physical properties, J. Alloys Compd. 743 (Apr. 2018) 146–154, https://doi.org/10.1016/j.jallcom.2018.01.396.

[85] M.A. Ali, S.H. Naqib, Recently synthesized $(Ti_{1-X}\ Mo_x)_2AlC$ ($0 \leq x \leq 0.20$) solid solutions: deciphering the structural, electronic, mechanical and thermodynamic properties via ab initio simulations, RSC Adv. 10 (52) (2020) 31535–31546, https://doi.org/10.1039/d0ra06435a.

[86] H. Ledbetter, A. Migliori, H. Ledbetter, A. Migliori, A General Elastic-Anisotropy Measure A General Elastic-Anisotropy Measure vol. 063516, 2006, pp. 1–6, https://doi.org/10.1063/1.2338835.

[87] M.A. Ali, M.W. Qureshi, Newly synthesized MAX phase Zr_2SeC: DFT insights into physical properties towards possible applications, RSC Adv. 11 (28) (2021) 16892–16905, https://doi.org/10.1039/D1RA02345D.

[88] C. Lee, X. Gonze, Ab initio calculation of the thermodynamic properties and atomic temperature factors of SiO_2 α-quartz and stishovite, Phys. Rev. B 51 (13) (Apr. 1995) 8610–8613, https://doi.org/10.1103/PhysRevB.51.8610.

[89] O.L. Anderson, A simplified method for calculating the debye temperature from elastic constants, J. Phys. Chem. Solid 24 (7) (Jul. 1963) 909–917, https://doi.org/10.1016/0022-3697(63)90067-2.

[90] Y. Zhou, H. Xiang, X. Lu, Z. Feng, Z. Li, Theoretical prediction on mechanical and thermal properties of a promising thermal barrier material: $Y_4Al_2O_9$, J. Adv. Ceram. 4 (2) (Jun. 2015) 83–93, https://doi.org/10.1007/s40145-015-0140-6.

[91] M.A. Ali, M.M. Hossain, M.M. Uddin, A.K.M.A. Islam, S.H. Naqib, Understanding the improvement of thermo-mechanical and optical properties of 212 MAX phase borides Zr_2AB_2 (A = In, Tl), J. Mater. Res. Technol. 15 (Nov. 2021) 2227–2241, https://doi.org/10.1016/j.jmrt.2021.09.042.

[92] S. Islam, M.R. Rana, P. Das, K. Hoque, S.H. Naqib, M.A. Ali, DFT insights into i-MAB phase, $Mo_4Y_2Al_3B_6$: a potential thermal barrier coating and solar heat reducing material, Phys. Scr. 99 (5) (Apr. 2024) 55975, https://doi.org/10.1088/1402-4896/ad3d90.

[93] M.A. Ali, M.M. Hossain, A.K.M.A. Islam, S.H. Naqib, Ternary boride Hf_3PB_4: insights into the physical properties of the hardest possible boride MAX phase, J. Alloys Compd. 857 (Mar. 2021) 158264, https://doi.org/10.1016/j.jallcom.2020.158264.

[94] D.T. Morelli, G.A. Slack, S.L. Shindé, J.S. Goela, High thermal conductivity materials, in: High Lattice Thermal Conductivity Solids, Springer, 2006.

[95] C.L. Julian, Theory of heat conduction in rare-gas crystals, Phys. Rev. 137 (1A) (Jan. 1965) A128–A137, https://doi.org/10.1103/PhysRev.137.A128.

[96] T. Tâm, N.C.Ứ.U. Và, C.Ê.N. Giao, C. Ngh, Â.N.B.Ụ.I. Chu, High Thermal Conductivity Materials vol. 01, Springer-Verlag, New York, 2006, https://doi.org/10.1007/b106785.

[97] W. Other, O.F. Poissonvs, O.F. Pure, C-05-1, in: J. Grunewald (Ed.), CESBP Central European Symposium on Building Physics/BauSIM 2016, Fraunhofer IRB Verlag, 2016, pp. 277–284, https://doi.org/10.51202/9783816797982-277.

[98] D.R. Clarke, Materials selections guidelines for low thermal conductivity thermal barrier coatings, Surf. Coatings Technol. 163–164 (2003) 67–74, https://doi.org/10.1016/S0257-8972(02)00593-5.

[99] Y. Liu, et al., Discovery of ABO_3 perovskites as thermal barrier coatings through high-throughput first principles calculations, Mater. Res. Lett. 7 (4) (Apr. 2019) 145–151, https://doi.org/10.1080/21663831.2019.1566183.

[100] B. Liu, et al., Advances on strategies for searching for next generation thermal barrier coating materials, J. Mater. Sci. Technol. 35 (5) (May 2019) 833–851, https://doi.org/10.1016/j.jmst.2018.11.016.

[101] B. Liu, J.Y. Wang, F.Z. Li, Y.C. Zhou, Theoretical elastic stiffness, structural stability and thermal conductivity of $La_2T_2O_7$ (T=Ge, Ti, Sn, Zr, Hf) pyrochlore, Acta Mater. 58 (13) (Aug. 2010) 4369–4377, https://doi.org/10.1016/j.actamat.2010.04.031.

[102] K. Bobzin, N. Bagcivan, T. Brögelmann, B. Yildirim, Influence of temperature on phase stability and thermal conductivity of single- and double-ceramic-layer EB–PVD TBC top coats consisting of 7YSZ, $Gd_2Zr_2O_7$ and $La_2Zr_2O_7$, Surf. Coatings Technol. 237 (Dec. 2013) 56–64, https://doi.org/10.1016/j.surfcoat.2013.08.013.

[103] B.J. Kennedy, Q. Zhou, M. Avdeev, Neutron diffraction studies of $Gd_2Zr_2O_7$ pyrochlore, J. Solid State Chem. 184 (7) (Jul. 2011) 1695–1698, https://doi.org/10.1016/j.jssc.2011.04.003.

[104] M.A. Ali, N. Jahan, A.K.M.A. Islam, Sulvanite compounds Cu_3TMS_4 (TM = V, Nb and Ta): elastic, electronic, optical and thermal properties using first-principles method, J. Sci. Res. 6 (3) (Aug. 2014) 407–419, https://doi.org/10.3329/jsr.v6i3.19191.

[105] A. Settouf, H. Rached, N. Benkhettou, D. Rached, DFT calculations of structural, optoelectronic and thermodynamic properties of $B_xAl_{1-x}P$ alloys, Comput. Condens. Matter 19 (Jun. 2019) e00377, https://doi.org/10.1016/j.cocom.2019.e00377.

[106] M.A. Ali, M.M. Hossain, M.M. Uddin, A.K.M.A. Islam, S.H. Naqib, The rise of 212 MAX phase borides: DFT insights into the physical properties of Ti_2PB_2, Zr_2PbB_2, and Nb_2AB_2 [A = P, S] for thermomechanical applications, ACS Omega 8 (1) (Jan. 2023) 954–968, https://doi.org/10.1021/acsomega.2c06331.

[107] S. Li, R. Ahuja, M.W. Barsoum, P. Jena, B. Johansson, Optical properties of Ti_3SiC_2 and Ti_4AlN_3, Appl. Phys. Lett. 92 (22) (Jun. 2008) 90–93, https://doi.org/10.1063/1.2938862.

[108] X. Li, H. Cui, R. Zhang, Structural, optical, and thermal properties of MAX-phase Cr_2AlB_2, Front. Phys. 13 (2) (Apr. 2018) 136501, https://doi.org/10.1007/s11467-017-0743-1.

[109] K. Rajesh, P. Krishnan, A. Mani, K. Anandan, K. Gayathri, P. Devendran, Physical strength and Opto-electrical conductivity of L-Serine Phosphate single crystal for structural and photonics devices fabrication, Mater. Res. Innov. 24 (5) (Jul. 2020) 295–300, https://doi.org/10.1080/14328917.2019.1664178.

[110] S. Al-Qaisi, et al., First-principles calculations to investigate electronic, structural, optical, and thermoelectric properties of semiconducting double perovskite Ba_2YBiO_6, Micro and Nanostructures 170 (March) (2022) 207397, https://doi.org/10.1016/j.micrna.2022.207397.

[111] S. Al-Qaisi, et al., First-principles investigations of Na_2CuMCl_6 (M = Bi, Sb) double perovskite semiconductors: materials for green technology, Mater. Sci. Semicond. Process. 150 (November 2021) (2022), https://doi.org/10.1016/j.mssp.2022.106947.

[112] H. Rached, S. Bendaoudia, D. Rached, Investigation of Iron-based double perovskite oxides on the magnetic phase stability, mechanical, electronic and optical properties via first-principles calculation, Mater. Chem. Phys. 193 (Jun. 2017) 453–469, https://doi.org/10.1016/j.matchemphys.2017.03.006.

[113] W.A. Dujana, et al., Structural, electronic, mechanical, thermal, and optical properties of UIr_3 under pressure: a comprehensive DFT study, AIP Adv. 11 (10) (Oct. 2021), https://doi.org/10.1063/5.0064021.

[114] M.W. Qureshi, M.A. Ali, X. Ma, Screen the thermomechanical and optical properties of the new ductile 314 MAX phase boride Zr_3CdB_4: a DFT insight, J. Alloys Compd. 877 (Oct. 2021) 160248, https://doi.org/10.1016/j.jallcom.2021.160248.

[115] S. Mohanty, S. Ghosh, S. Nayak, A.P. Das, Isolation, identification and screening of manganese solubilizing fungi from low-grade manganese ore deposits, Geomicrobiol J. 34 (4) (2017) 309–316, https://doi.org/10.1080/01490451.2016.1189016.

[116] S. Mishra, R.P. Singh, C.C. Rath, A.P. Das, Synthetic microfibers: source, transport and their remediation, J. Water Process Eng. 38 (April) (2020) 101612, https://doi.org/10.1016/j.jwpe.2020.101612.

[117] K. Raj, A.P. Das, Lead pollution: impact on environment and human health and approach for a sustainable solution, Environ. Chem. Ecotoxicol. 5 (December 2022) (2023) 79–85, https://doi.org/10.1016/j.enceco.2023.02.001.

[118] D.R. Hussein, K.K. Abbas, A.M.H.A. Al-Ghaban, Overview of structural, electronic, elastic, thermal, optical, and nuclear properties of Zr_2AC (A= Al, Si, P, S, Ge, As, Se In, Sn, Tl, and Pb) MAX phases: a brief review, Heliyon 9 (8) (2023) e18303, https://doi.org/10.1016/j.heliyon.2023.e18303.

[119] V. Srinivasan, T.H. Rana, First principle insights into the physical properties of Ti-based 211-MAX phase nitrides Ti_2AN (A = Tl and Pb), Phys. Scr. 98 (11) (Oct. 2023) 115944, https://doi.org/10.1088/1402-4896/acfffe.

[120] D. Hussein, K. Abbas, A. Abdulkadhim Al-Ghaban, Overview in technical synthesis and applications of Zr_2AC (A= In, Sn, Pb, Al, S and Se) MAX phases: a brief review, Eng. Technol. J. 41 (6) (2023) 1–15, https://doi.org/10.30684/etj.2022.136391.1313.